



**MULTIPLICATOR DISCHARGE IN HIGH
POWER MICROWAVE SYSTEMS:
ANALYZING EFFECTS AND MITIGATION
THROUGH SIMULATION IN ICEPIC**

THESIS

Robert Lloyd, 2nd Lieutenant, USAF
AFIT-ENP-13-M-22

**DEPARTMENT OF THE AIR FORCE
AIR UNIVERSITY**

AIR FORCE INSTITUTE OF TECHNOLOGY

Wright-Patterson Air Force Base, Ohio

Approved for public release; distribution unlimited.

The views expressed in this thesis are those of the author and do not reflect the official policy or position of the United States Air Force, Department of Defense, or the United States Government. This material is declared a work of the U.S. Government and is not subject to copyright protection in the United States.

AFIT-ENP-13-M-22

MULTIFACTOR DISCHARGE IN HIGH POWER MICROWAVE SYSTEMS:
ANALYZING EFFECTS AND MITIGATION THROUGH SIMULATION IN
ICEPIC

THESIS

Presented to the Faculty
Department of Engineering Physics
Graduate School of Engineering and Management
Air Force Institute of Technology
Air University
Air Education and Training Command
in Partial Fulfillment of the Requirements for the
Degree of Master of Science in Engineering Physics

Robert Lloyd, BS
2nd Lieutenant, USAF

March 2013

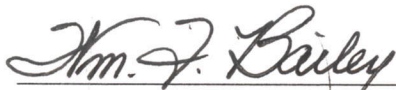
Approved for public release; distribution unlimited.

AFIT-ENP-13-M-22

MULTIFACTOR DISCHARGE IN HIGH POWER MICROWAVE SYSTEMS:
ANALYZING EFFECTS AND MITIGATION THROUGH SIMULATION IN
ICEPIC

Robert Lloyd, BS
2nd Lieutenant, USAF

Approved:



William F. Bailey (Chairman)



Date



Robert B. Greendyke (Member)



Date



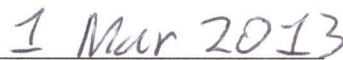
Nathaniel P. Lockwood (Member)



Date



David E. Weeks (Member)



Date

Abstract

Single surface multipactor in high power microwave systems was investigated computationally and analytically. The research focused upon understanding the cause and parametric dependence of the multipactor process leading to suggested methods of mitigation. System damage due to reflection was also assessed. All simulations were performed using the PIC code developed by AFRL, known as ICEPIC. In recreating the susceptibility curves that define regions of multipactor growth and decay, a discrepancy was found between previous published results and those observed in the current simulation. This was attributed to previous simulations not accounting for the magnetic component in the electromagnetic radiation incident on the dielectric window. By surveying different static magnetic and electric fields both parallel and perpendicular to the dielectric, revised susceptibility curves were determined. An analytic method confirmed the origin of the discrepancy. The reflection of the waveguided radiation by the multipactor electrons degrades the output and may damage the microwave source. A theory for the reflection resulting from multipactor was derived to aid in quantifying reflection. A plane wave was used to model incoming microwave radiation and the amplitude of the electric field in reflected and transmitted waves was measured for various frequencies of the incident plane wave.

Acknowledgements

First of all, I am most grateful to God and his son for their relationship during this time of trouble. I know that without their help, I would have never had the strength or endurance to finish the assignment set before me. I would also like to thank Dr. Bailey, my advisor, who also worked to help me complete the work while also instilling in me a sense of how to conduct actual research. He has always had an open door policy, allowing me to receive help while also motivating further thought into the process behind multipactor. I know that science is a continuous process whereby my progress is highly dependent upon the hard work completed by the people who have come before me. No one illustrates this better than Dr. Bailey.

I would also like to thank Dr. Lockwood and the research group at Kirtland Air Force Base. Both for their assistance in sponsoring the research of multipactor mitigation and in the guidance in understanding simulation and evaluating the multipactor phenomenon with ICEPIC. I would also like to thank my fellow AFIT students, for their words of encouragement and honest evaluation of the work. As well as their helping me formulate my descriptions of multipactor used throughout the thesis and in the defense.

I would also like to thank my family, my mother for giving me encouragement in the throughout this process. My father, for giving perspective to the Master's Thesis writing process and advice in defending the research. Finally, I would like to thank my future wife, for her patience and encouragement that gave me a "cold cup" of water while journeying towards my final end goal of graduation.

Robert Lloyd

Table of Contents

	Page
Abstract	iv
Acknowledgements	v
List of Figures	viii
List of Tables	ix
List of Symbols	x
List of Abbreviations	xi
I. Introduction	1
1.1 Purpose	1
1.2 Problem Description	3
1.3 Goals of the Research	3
1.4 Background	4
1.5 Definition of Terms	6
1.6 PIC Code	7
1.7 Consistency of PIC Methods	8
Simulation Setup	9
II. Understanding Multipactor: Susceptibility Mapping	12
2.1 Theory	12
Secondary Electron Emission	12
Initiation of Multipactor	15
Analytic Solution for Determining Boundary Curves with an Oscillating Electric Field	16
Analytic Solution for Determining Boundary Curves with Static Magnetic and Electric Fields	19
2.2 Method	21
Defining the EM Radiation	22
Particle Emission	22
Static Field Implementation	24
Building Susceptibility Curves	24
2.3 Results and Analysis	25
III. Analysis and Simulation of Reflection	31
3.1 Theory	31
Understanding Multipactor in Real Time	31

	Page
Calculating the Power Transmitted through the Multipactor	33
Calculating the Intensity Reflected	39
3.2 Methodology	40
Reflection of the Dielectric Window	40
Using PROBE to Determine Electric Fields	41
Using Particle Count to Determine Electric Field Perpendicular	44
Particle Weighting	45
3.3 Results and Analysis	47
IV. Conclusions and Future Work	49
4.1 Conclusions	49
4.2 Future Work	50
Bibliography	52
Vita	54

List of Figures

Figure	Page
1. Electron Avalanche	5
2. The PIC Cycle	8
3. Simulation Specifications	10
4. Emission Trajectory	13
5. Electron Secondary Curve	14
6. Secondary Emission Curve indicating Multipactor Growth and Decay	15
7. Example Susceptibility Diagram	17
8. Plane Wave Shape	23
9. Generating a Boundary Curve	25
10. Particle Counts for Boundary Curve Generation	26
11. Results Previously Reported in the Literature	27
12. Remapping of the Susceptibility Diagram	28
13. Static Field Observed Boundary Curve Shift	29
14. Boundary Curve Shift Based on Theory	30
15. Dynamic Particle Growth in Multipactor	32
16. Parametric plot of E_{\parallel} and E_{\perp} in SC Case	33
17. Plot of the Transmission Coefficient	39
18. Probe Layout in Simulation	42
19. E_{\perp} Measurement with PROBE Line	43
20. E_{\perp} Measurement with Particle Counts	44

List of Tables

Table		Page
1.	Parameters used for NSC simulations	24
2.	Boundary Condition Studies for the Magnetic Field Case	29
3.	Parameters used for SC simulations	43
4.	Values Received for Weighting Tests	46
5.	Results from Reflect	48

List of Symbols

Symbol	Page
E	Electric field 6
B	Magnetic Induction 6
ε	Energy associated with the free electrons 6
ω	Angular frequency of wave incident on the dielectric 6
m	Symbol for mass 6
q	Symbol for charge 6
E_{RF}	Electric field associated with the incident microwave 7
E_{\parallel}	Electric field parallel to the dielectric surface 7
E_{DC}	Bias field associated with charge on the surface of the dielectric 7
E_{\perp}	Field that is perpendicular to the dielectric surface 7

List of Abbreviations

Abbreviation		Page
DoD	Department of Defense	1
PIC	Particle-in-Cell	6
NSC	Non-Space Charge	6
SC	Space Charge	6
ICEPIC	Improved Concurrent Electromagnetic Particle-in-Cell	7
AFRL	Air Force Research Laboratory	7
PML	Perfectly Matched Layer	9

MULTIPACTOR DISCHARGE IN HIGH POWER MICROWAVE SYSTEMS:
ANALYZING EFFECTS AND MITIGATION THROUGH SIMULATION IN
ICEPIC

I. Introduction

1.1 Purpose

The DoD interest in researching microwave technology began in the early 1930s and substantially increased during World War II due to the rise of radar technology utilized by the Allied powers throughout the war [4]. After the war, many of the processes developed with higher power radar systems led to many commercial uses of microwaves in fields of communication, navigation, spectroscopy and radiative power transfer [18] [7]. Even though the private sector has made ample use of microwave technology since the end of World War II, the Department of Defense still employs research in the development of microwave systems in the furtherance of tactical and strategic capabilities [4, p. 8]. In 1975, experiments conducted by both the Naval Research Laboratory and Cornell led to the development of free electron MASERS capable of generating 1 GW in the X-band of the microwave spectrum

The most recent DoD research regarding microwave weapons follows along the lines of the Air Force Scientific Advisory Board's New World Vistas statement:

“Promising present-day research in high power microwave (HPM) technology allows us to envision a whole new range of compact weapons that will be highly effective in the sophisticated, electronic battlefield environment of the future. There are many advantages of these HPM weapons:

First, there are virtually no target acquisition, pointing, and tracking requirements in any HPM weapon employment scenario. Electromagnetic (EM) radiation, traveling at the speed of light, will envelop a large volume that can engage multiple targets at once. HPM weapons could be used in nearly all weather, although frequencies above 10 GHz degrade somewhat. Some HPM weapons designs could be employed in a covert way since the beam is not visible and the damage and/or upset could be directed to electronic targets. Since in many applications the only expendable is fuel for electrical generators, HPM weapons are expected to come with a large “magazine.” It may be possible to design a system that acts as both radar and weapon, which first detects and tracks the target than increases the power and engages the target, all at electronic speeds, Finally, a distinct advantage of HPM lies in the fact that it may be considered a nonlethal weapon that would prevent the enemy from using his electronic equipment successfully with no impact on human life. [1].”

This quote illustrates the importance of HPMS to modern military operations. However, it does not mention the technological hurdles that must first be crossed before such benefits can be realized by the modern warfighter. The Defense Technology Area Plan lists these required developments for the success of HPM weapons [2]:

1. Compact, high-peak-power or high-average-power HPM sources.
2. Compact, high-gain, ultra-wideband antennas
3. Compact, efficient, high-power,pulsed power drivers.
4. Compact, efficient prime power sources.
5. Predictive models for HPM effects and lethality
6. Low-impact hardening of systems hostile and self-induced Electro-Magnetic Interference
7. Affordable system integration meeting military platform requirements.

1.2 Problem Description

This research focused on improving items 1 and 2 of the technology plan by analyzing the source initiated secondary electron emission from the dielectric window that separates the interior of the HPM waveguide from the atmosphere. Thermal and mechanical window failure compromises the vacuum integrity of the microwave system and limits the maximum output power.

Current thought concerning HPM window damage indicates the cause stems from thermodynamic effects due to the formation of multipactor along the cell window [13]. Multipactor is characterized by the creation of an electron cascade along the inside of the waveguide window in the presence of high amplitude microwave radiation, thereby creating plasma inside the waveguide vacuum. The presence of plasma not only damages the window through thermodynamic effects, but also leads to second order effects that end up damaging the entire HPM system. For example, the reflection of EM radiation by the multipactor tends to damage the HPM source and lowers the power output of the entire system.

1.3 Goals of the Research

This research focused on the characterization of multipactor with the intended end result of identifying methods of mitigation of secondary electron growth. In order to work towards these end results, multipactor initiation was surveyed to better understand under what circumstances multipactor growth and decay occur. Power balance was analyzed and an analytic development of reflection was developed

1.4 Background

In 1934 Otto Farnsworth was the first to recognize the phenomenon of multipactor discharge. He named the phenomenon after the effects he observed in his invention, the “AC electron multipactor” [19]. Multipacting was also observed in many other gaseous breakdown experiments and was characterized by Abraham, Sperry Gyroscope engineers, and by Forrer and Milazzo in 1950’s [23]. Due to the lack of information regarding the dynamics of secondary electron emission, Vaughan extended theoretical knowledge of secondary electron emission with empirical formula characterizing electron emission from a surface as a function of impact electron energy and angle [24].

With Vaughan’s empirical model, the process behind multipactor becomes clear. The multipactor process follows from an initial seed electron impacting the dielectric and causing secondary electron emission. These secondary electrons, then being ejected from the surface, are accelerated by the parallel electric field associated with microwave radiation. The electrons are then returned to the surface by either a perpendicular bias electric field, the positive charge on the dielectric window left by the secondary emitted electrons, or the magnetic field component of the microwave radiation propagating through the window. The acceleration from the microwave radiation results in an increase in the electron’s kinetic energy during its flight in the waveguide before impacting the window. If the particle’s kinetic energy is great enough, the impacting electron will cause more electrons to be emitted. For high electric field amplitudes this process results in an avalanche of electrons on the outside of the waveguide dielectric window. An illustration of this process can be seen in Figure 1.

Previous work in this field has been focused on the analysis of window breakage in HPM systems, with experimental analysis performed at Texas Tech University. These experiments focused on characterizing dielectric window breakdown in the presence

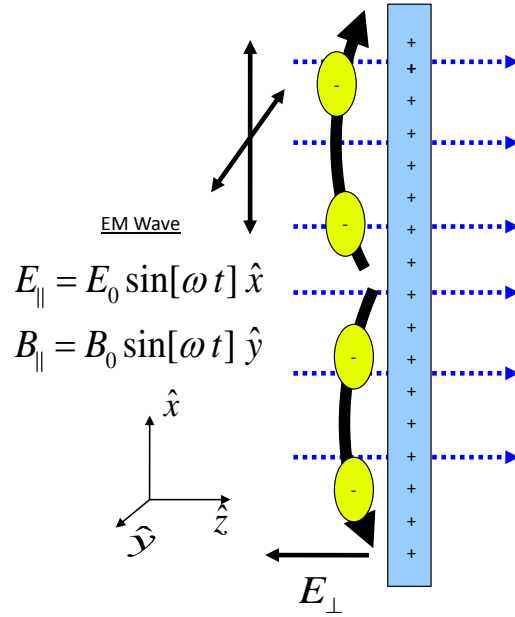


Figure 1. The multipactor effect on a waveguide window. Electrons are emitted from the vacuum side of the dielectric window and are pulled back to the window due to the formation of a positive charge (with a field labeled as E_{\perp}) and gain energy from the electromagnetic field (labeled as E_{\parallel}).

of high intensity microwave radiation [4]. The laboratory experiments performed by Texas Tech also observed the multipactor discharge along the dielectric window through x-ray emission, discharge luminosity, and microwave fields [16]. Other studies performed over the past few years have also indicated that the magnetic fields play a large effect in determining electron transit time [11].

Computational work has also joined the research effort, being cost effective and a vehicle to understanding the fundamental physics involved in the multipactor process. Monte Carlo techniques were originally used to process the electron avalanche through the simulation of an oscillating E_{\parallel} field representing the electric field component of incoming microwave radiation, and a static E_{\perp} field representing either the return field associated with space charge present on the dielectric window or an imposed bias

[13]. Electron avalanche was accurately modeled with Vaughan formula for secondary electron yield [8]. Experimental research performed at Texas Tech [16] showed that space charge must be included to properly characterize the multipactor evolution [22]. This has led to the use of Particle-in-Cell (PIC) methods for modeling of dielectric window systems [19] [20].

1.5 Definition of Terms

Before delving into the research accomplished, it is important to characterize two of the different situations observed throughout the simulations. One in which space charge, the charge associated with the electrons and the positive charge contribution from the dielectric, is ignored. This case will be referred to as the Non-Space Charge (NSC) case. The Space Charge (SC) case is characterized by the allowance of particle growth and decay through the self-consistent inclusion of the electron's effects on each other and the effects of the positive charge on the surface of the dielectric.

Before proceeding, basic definitions of relevant physical quantities and their corresponding symbols are provided.

- An E symbol stands for the electric field and B stands for the magnetic field.
- An ε indicates energy associated with the free electrons
- An ω indicates angular frequency.
- The physical constants of mass and charge are written as m and q respectively.
- These definitions may be further modified by the use of subscripts indicating the association of the physical quantity with either a direction or object within the system. For example, the symbol q_e indicates the charge of an electron and the symbol v_z indicates the component of the velocity in the \hat{z} direction.
- Some of the symbols used throughout the paper will be different than the

conventional ones used throughout much of the literature due to improvements in the understanding of the multipactor process.

- Throughout the paper E_{RF} field symbol will be replaced with the symbol E_{\parallel} in representing the E field parallel to the window. This admits treatments of oblique incidence where the E_{RF} field contributes components parallel and perpendicular to the dielectric window.
- The E_{DC} will be replaced with the symbol E_{\perp} , representing the E field perpendicular to the window. This change is due to the the electric field associated with the positive charge on the dielectric window dynamically evolving as a function of particles in the SC case and accommodates the oblique incidence condition

Further definitions of symbols will be discussed as they occur in the paper.

1.6 PIC Code

This section outlines the use of the PIC code used in modeling the movements of particles within the system used throughout all of the research. Particle-in-cell methods work by tracking individual particles in a continuous space, but treats the calculations of their field elements as functions of both current and particle densities per cell. This method is efficient because by representing a large number of particles as a single large pseudo particle, the physics of a problem may be better understood while increasing the efficiency of a simulation. The typical PIC algorithm operates in a four step cycle, in which the particle, field interactions, and energy exchanges are treated self-consistently. An illustration of the cycle can be found in Figure 2. For this research, the Improved Concurrent Electromagnetic Particle-in-Cell (ICEPIC) was chosen in modeling the system. ICEPIC is a self consistent and fully relativistic modeling software developed by Air Force Research Laboratory (AFRL) [5] to aid in

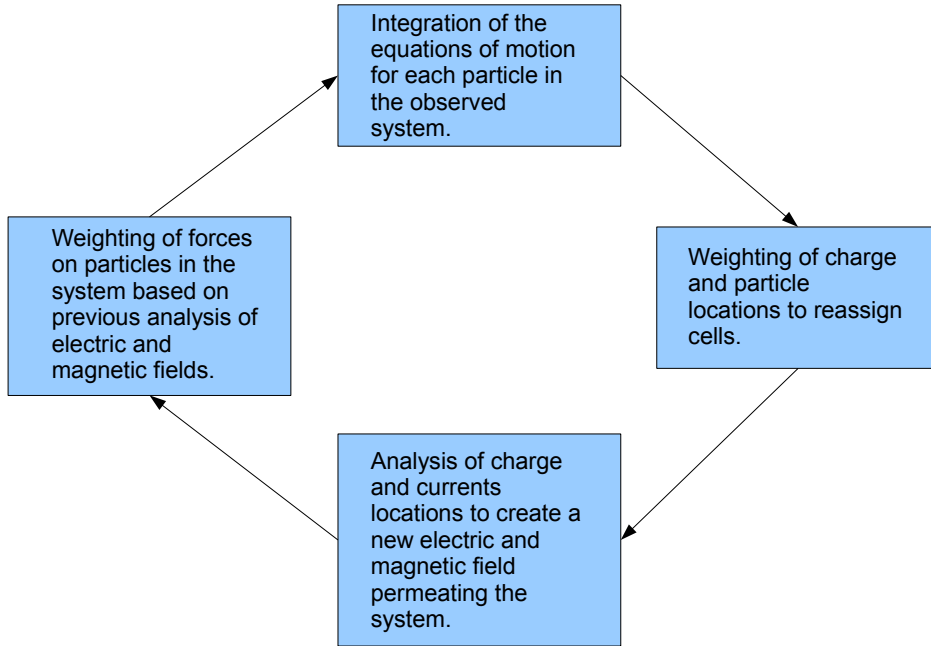


Figure 2. The four step PIC algorithm illustrating the process of taken by the PIC code for every iteration.

the development of HPM devices.

1.7 Consistency of PIC Methods

Even though PIC methods grant insight of the physics behind a system, PIC operations require that a few conditions must be met in order for accurate results of systems to be observed. One such constraint involves the time step (dt) of the simulation. Normally, the thermal velocity of the particles necessitates the size of the time step must be less than $\frac{dz}{v}$, where dz is the spatial size of the grid and v is the velocity of thermal velocity of an electron. When considering fully coupled electrodynamic simulations, the requisite velocity is the speed of light. Therefore, the

simulation timestep is

$$dt = \frac{0.99dz}{\sqrt{2}c}, \quad (1)$$

where c is the speed of light.

Another constraint requires that the grid scale resolve structures smaller than the Debye length associated with the multipactor plasma and is complemented by the additional statistical requirement that each cell in the simulation containing at least 5-10 particles [6]. Previous results in meeting these requirements have yielded data that agree with analytic theory [13][19].

Simulation Setup.

The default material of the ICEPIC environment is a perfect conductor. Vacuum within the system must be carved out of this conductor allowing for the simulation of an environment comparable to the inside of a microwave waveguide. The simulated geometry model used follows the model described both by Fichtl [8] and Rogers [19] and is displayed in Figure 3 .

The Perfectly Matched Layer (PML) of the simulation acts as perfect absorbers of the plane wave moving through the waveguide. Another important feature in the simulation is the inclusion of a secondary dielectric that prevents emitted high energy particles from interacting with the plane wave emitter on the $-\hat{z}$ side of the simulation. Finally, a periodic boundary condition is also included along the waveguide, meaning that any particles traversing the boundary shall return on the other side of the periodic boundary of the system. This allows for a smaller simulation grid-space to be used, while still maintaining the particle rich environment of the simulation.

In order for the system to maintain a consistent resolution while varying the frequencies used in the simulation, dz is made to be dependent on wavelength divided by a resolution constant (factors of 3000 for when space charge is not included and

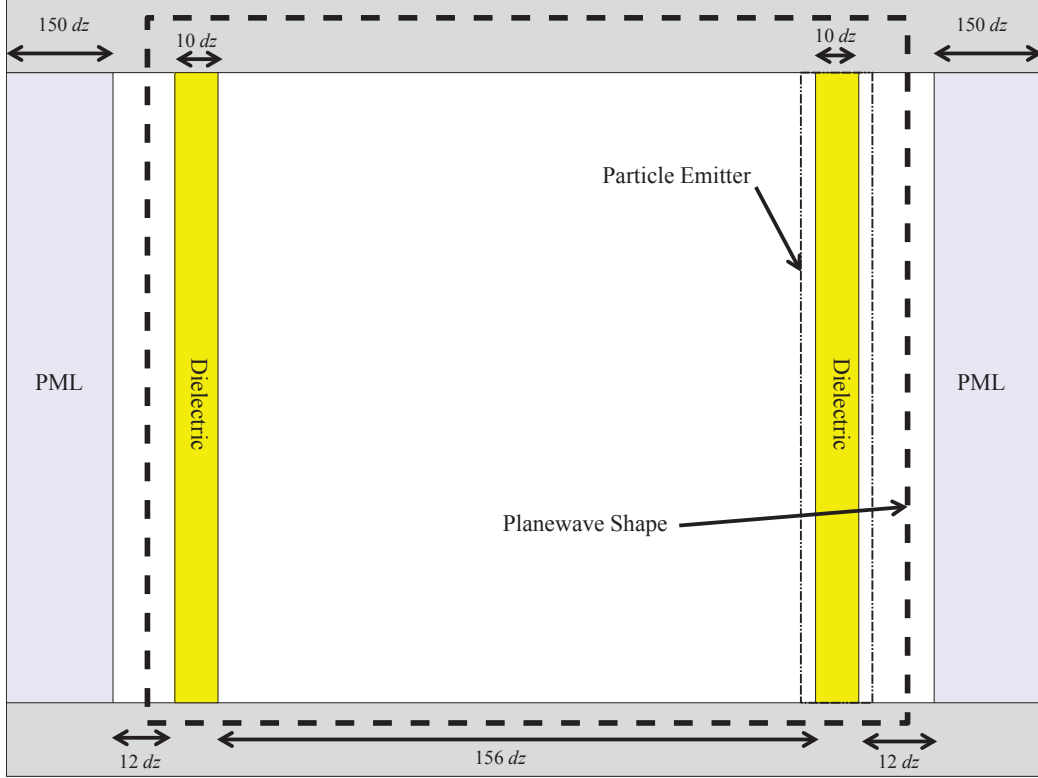


Figure 3. Simulation geometry following Fichtl [8] and Rogers [19].

12000 for when space charge is included in the simulation). This difference in resolution was based upon previous work done by Fichtl [8], and comes from the previous requirement to maintain the particle dynamics by constraining the grid size to be smaller than a Debye length [8].

For most ICEPIC simulations, the frequency of the sinusoidal oscillations of the electric and magnetic fields was $2.45 GHz$. For the case where space charge is treated, nominal specifications of the system were

$$dz = \frac{\lambda}{12000} \approx 1.02 \times 10^{-5} m \quad (2)$$

$$\Delta x_{Full} = Nx \times dz \approx 7.10 \times 10^{-5} m \quad (3)$$

$$\Delta z_{Particle\ Space} = 156 \times dz \approx 1.59 \times 10^{-3} m \quad (4)$$

$$\Delta z_{PML\ Depth} = 150 \times dz \approx 1.53 \times 10^{-3} m \quad (5)$$

$$\Delta z_{Simulation\ Space} = Nz \times dz \approx 5.10 \times 10^{-3} m \quad (6)$$

as indicated in Figure 3.

The temporal resolution of the system depends on the value dz , so that the temporal resolution may be treated as a function of frequency and resolution,

$$dt = \frac{0.99dz}{\sqrt{2}c} \quad (7)$$

$$dt = \frac{0.99\lambda}{12000\sqrt{2}c} \quad (8)$$

$$dt = \frac{0.99}{12000\sqrt{2}f} \approx 2.38 \times 10^{-14} s \quad (9)$$

This time step value is roughly a factor of 17000 smaller than the period of the incoming wave, and on the order of one hundredth the transit time of the electron. Therefore, the simulation accurately model the physics associated with a real microwave system.

II. Understanding Multipactor: Susceptibility Mapping

A susceptibility diagram is a parametric map of regions of growth and decay in the space defined by E_{\parallel} and E_{\perp} . This is a logical choice because the injected electron gains energy primarily from the parallel component of the microwave field while the perpendicular component determines the time of flight. In mapping the susceptibility diagram for multipactor initiation, the simulations focused on the NSC case. Considering the differences in implementation of the NSC and SC in both theory and in the ICEPIC simulation it is convenient to treat the mapping of the initiation of multipactor growth and decay in this chapter and reserve the analysis of multipactor dynamics and power balance to Chapter III.

2.1 Theory

Secondary Electron Emission.

Vaughan's emission curves allow for empirical modeling of the secondary electron yield from data produced by others, such as Gibbons [24]. The geometry of the dielectric surface on which this modeling is based is shown in Figure 4.

For this configuration the ratio of secondary emitted electrons to incident electrons (δ) in terms of the angle of impact (ς) is

$$\delta(\varepsilon_i, \varsigma) = \begin{cases} \delta_{max}(\varsigma) \cdot (w \exp((1-w)))^{k(w)} & \text{for } w \leq 3.6 \\ \delta_{max}(\varsigma) \cdot (1.125w^{-0.35}) & \text{for } w > 3.6. \end{cases} \quad (10)$$

Where $w = \frac{\varepsilon_i}{\varepsilon_{max}(\varsigma)}$, and the corrected maximum electron emission energy is given by

$$\varepsilon_{max}(\varsigma) = \varepsilon_{max0} \cdot \left(1 + \frac{k_s \varsigma^2}{\pi}\right). \quad (11)$$

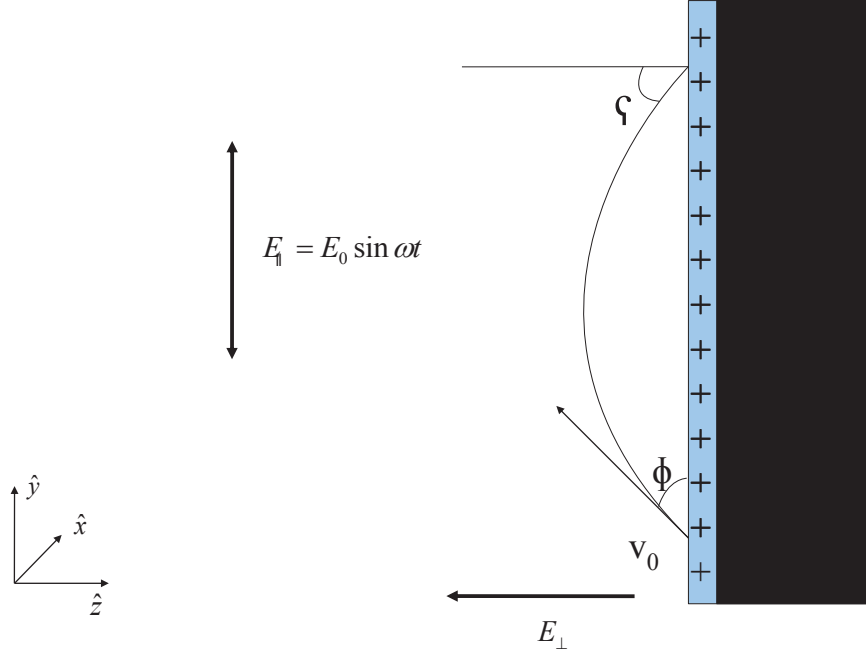


Figure 4. Trajectory of the secondary electron. v_0 is the electrons initial energy, ϕ is the electron's initial emission angle, and ς is the angle at which the particle impacts the dielectric surface.

The corrected maximum emission term in respect to the impact angle to the surface may be written as

$$\delta_{max}(\varsigma) = \delta_{max0} \cdot \left(1 + \frac{k_s \varsigma^2}{2\pi}\right). \quad (12)$$

In both of these equations k_s is the smoothness parameter of the system (usually set equal to 1 [19]). ε_{max0} and δ_{max0} are constants dependent on properties of the material and may be altered to effect secondary electron emission. In Equation 10, $k(w)$ is also normally defined as either as a piecewise function of w :

$$k = \begin{cases} 0.56 & \text{for } w \leq 1 \\ 0.25 & \text{for } 1 < w \leq 3.6 \end{cases} \quad (13)$$

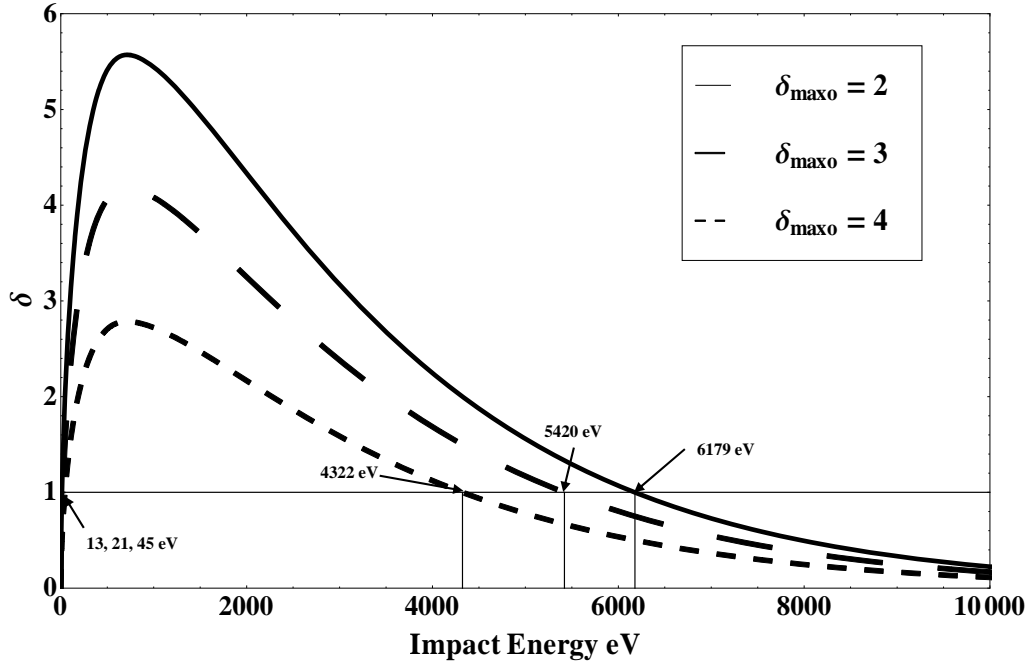


Figure 5. Emission yield vs Impact energy. The various curves represent different values for δ_{max0} , an input based on the dielectric window material. ε_1 and ε_2 are also known as the low and high crossover energies. This figure is based on the figures generated from Vaughan's equations[24].

or in terms of Valfells continuous representation of k in terms of w [22]:

$$k = 0.435 - \frac{0.27}{\pi} \arctan(\pi \ln(w)). \quad (14)$$

Figure 5 shows an example output of the function $\delta(\varepsilon_i, \varsigma)$, for different values of δ_{max0} , indicating the degree to which the secondary electron yield depends upon the material properties of the dielectric. The figure illustrates that the energy associated with electron impact dictates the secondary emission yield associated with particle impact. When $\delta > 1$ an electron impacting on the surface indicates that more than one electron is emitted for the impact. Likewise, when $\delta \leq 1$ the impacting electron is absorbed. Within the theoretical analysis, it was assumed that the impact angle is $\frac{\pi}{2}$ due to the large velocity component expected for motion in the \hat{x} direction due to the accelerating E_{\parallel} field. This means that for the research, only two impact energies were

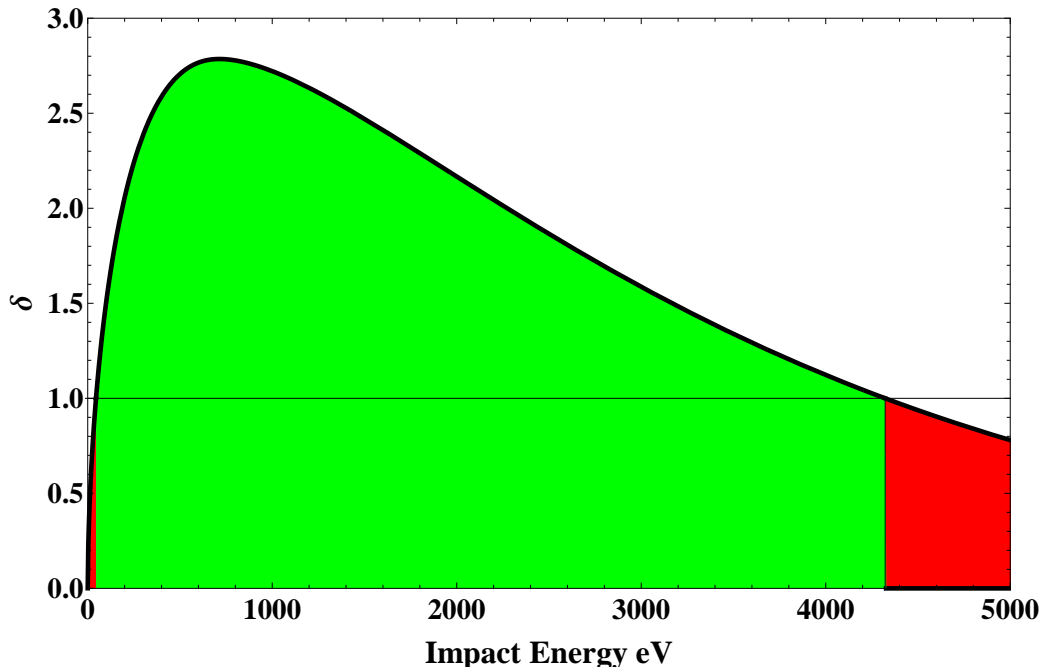


Figure 6. A colored secondary emission curve, where the color green indicates impact energies that lead to secondary particle growth and the color red corresponds to energies at which secondary particle growth will not occur.

considered for analytically determining whether the the impacting electron generates more electrons or gets absorbed. Therefore, the lower cutoff energy (labeled ε_1) and upper cutoff energy (labeled ε_2) determine a region of multipactor growth and decay.

Initiation of Multipactor.

The secondary emission curve indicates boundaries governed by the average energy of particle impact. If the average energy of the particles impacting the surface of the dielectric is greater than the energy at ε_1 and below the higher cutoff energy of ε_2 multipactor will be initiated within the system. Otherwise electrons will be absorbed and multipactor shall cease. These regions of the secondary emission curve are color coded in Figure 6. With the the microwave field (E_{\parallel}) acting as the sole energy provider to the electron, it becomes evident that multipactor initiation may be written in terms of the E_{\parallel} field. However, the E_{\perp} field must also be considered

for its role in returning the particle to the dielectric window. By writing the initial energy of the electron as a function of velocity ($\varepsilon_{m0} = \frac{1}{2}m_e v_i^2$) and considering only the E_{\perp} as the return force ($F_z = q_e E_{\perp}$), the time of flight [22] of the particle may be written as

$$\tau = \frac{\sqrt{2\varepsilon_{m0}m_e}}{q_e E_{\perp}}. \quad (15)$$

Assuming the energy gained is proportional to the time of flight, the secondary electron yield may be written as a function of both E_{\parallel} and E_{\perp} . This redefinition of secondary electron yield as being parametrically defined by the electric fields parallel and perpendicular to the dielectric surface yields a susceptibility diagram. An example susceptibility diagram is shown in Figure 7. Note that within the diagram the region of multipactor growth (shown in the figure as a green region) corresponds to energies between crossover energies ε_1 and ε_2 . The red region in the susceptibility diagram correspond to regions of particle decay. The lines on the example figure correspond to boundary curves, these are regions where the secondary electron yield is equal to one. $\delta = 1$ defines the boundary curves at which multipactor growth or decay occur. These boundary lines are important in determining the degree to which a bias field needs to be utilized to prevent multipactor initiation.

Analytic Solution for Determining Boundary Curves with an Oscillating Electric Field.

Previously, boundary curves have been created using the analytic expressions originally formulated by Valfell's in his initial treatment of characterizing multipactor growth [22]. This may be accomplished by deriving the electron energy gained during its flight in the E_{\parallel} field. By treating the E_{\parallel} field as a function $E_{\parallel} * \sin(\omega t + \theta)$ where ω is the angular frequency of the EM wave, θ is the emission phase, and E_{\parallel} is the

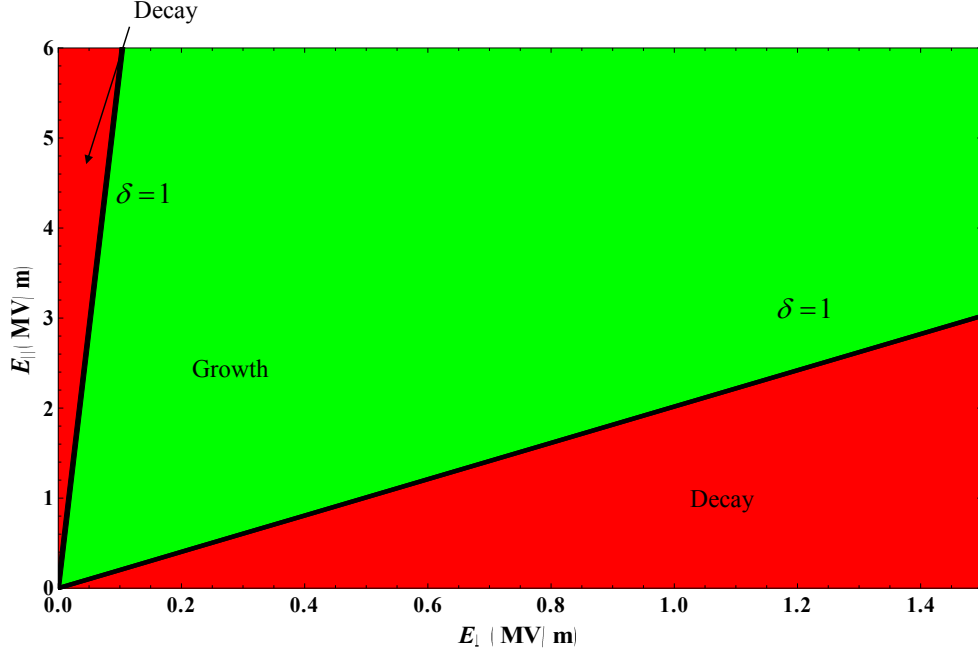


Figure 7. Susceptibility diagram for the NSC case. The regions are colored based on whether the region will initiate multipactor. Red indicating that multipactor shall not be initiated and green indicating that multipactor shall be initiated. These regions correspond to average impact energies graphed in Figure 6.

amplitude of the electric field, the equations of motion for the electron become

$$\ddot{y} = -\frac{eE_{\parallel}}{m_e} \sin[\omega t + \theta] \quad (16)$$

$$\ddot{z} = \frac{q_e}{m_e} E_{\perp}. \quad (17)$$

The energy gained by an electron during a complete time of flight is

$$\Delta\varepsilon_y = \frac{1}{2} m \dot{y}^2(\tau) - v_{0y}^2 \quad (18)$$

where $\Delta\varepsilon_y$ is the change in kinetic energy of the electron, v_{0y} is the electrons initial velocity perpendicular to the surface of the dielectric, and τ is the time of flight. By

combining this with the solution to equation 16, Equation 18 can be rewritten as

$$\Delta\varepsilon_y = \frac{v_{0y}q_e E_{\parallel}}{\omega} [\cos(\omega\tau + \theta) - \cos(\theta)] + \frac{e^2 E_{\parallel}^2}{2m_e\omega^2} [\cos(\omega\tau + \theta) - \cos(\theta)]^2. \quad (19)$$

When Equation 19 is averaged based on the emission phase, the average energy becomes

$$\langle\Delta\varepsilon_y\rangle = \frac{q_e^2 E_{\parallel}^2}{2m_e\omega^2} [1 - \cos(\omega\tau)] \quad (20)$$

where the electron time of flight (τ) was previously indicated in Equation 15. Assuming mono-energetic emission, where the electron emission energy equated to the average of the emission energy distribution [8], the electron transit time then becomes

$$\tau = \frac{4\sqrt{m_e\varepsilon_{0m}}}{q_e E_{\perp}}. \quad (21)$$

Inserting this value into Equation 20 yields the full energy gain

$$\langle\Delta\varepsilon_y\rangle = \frac{q_e^2 E_{\parallel}^2}{2m_e\omega^2} \left[1 - \cos \left[\frac{4\sqrt{m_e\varepsilon_{0m}}}{\frac{q_e E_{\perp}}{\omega}} \right] \right]. \quad (22)$$

and by adding this equation to the original injection energy (ε_{0m}) leads to an expression for the final impact energy on the dielectric

$$\varepsilon_{Impact} = \varepsilon_{0m} + \frac{q_e^2 E_{\parallel}^2}{2m_e\omega^2} \left[1 - \cos \left[\frac{4\sqrt{m_e\varepsilon_{0m}}}{\frac{q_e E_{\perp}}{\omega}} \right] \right]. \quad (23)$$

This may be rewritten as

$$\sqrt{\frac{2m_e\varepsilon_{Impact} - 2\varepsilon_{0m}m_e}{\left[1 - \cos \left[\frac{4\omega\sqrt{m_e\varepsilon_{0m}}}{q_e E_{\perp}} \right] \right]}} = \frac{q_e E_{\parallel}}{\omega} \quad (24)$$

By setting ε_{Impact} to crossover energies, the boundary curves associated with $\delta = 1$ may be determined. Equation 24 may be simplified by assuming $\sqrt{m_e \varepsilon_{0m}} \omega \ll q_e E_{DC}$ leading to

$$\sqrt{\frac{1 \frac{\varepsilon_{Impact}}{\varepsilon_{0m}} - 1}{8}} E_{DC} = E_{RF}. \quad (25)$$

This yields the linear relationship previously observed in boundary curves for the NSC cases reported by Fichtl and Rogers [8] [19].

Analytic Solution for Determining Boundary Curves with Static Magnetic and Electric Fields.

In order to corroborate findings found in remapping the susceptibility diagrams, it became important to also observe the effect of a magnetic field. Understanding that the electron transit time is much shorter than the period of the electromagnetic radiation, one may treat all of the fields associated with microwave energy as being static where the force equation is

$$\vec{F} = q_e \vec{E} + q_e (\vec{v} \times \vec{B}). \quad (26)$$

For this analytic development, the electric and magnetic fields associated with the electromagnetic radiation will be written as

$$B_{\parallel} = B_{RF} \quad (27)$$

$$E_{\parallel} = E_{RF} \quad (28)$$

and the bias field shall be written as

$$E_{\perp} = -E_{DC}. \quad (29)$$

The equations of motion associated with the trajectory of the electron are

$$\frac{d^2y}{dt^2}[t] = \frac{q_e}{m_e} \left(E_{RF} - B_{RF} \frac{dz}{dt} \right) \quad (30)$$

$$\frac{d^2z}{dt^2}[t] = \frac{q_e}{m_e} \left(-E_{DC} - B_{RF} \frac{dy}{dt} \right) \quad (31)$$

$$\frac{dy}{dt}[0] = v_0 \cos[\phi] \quad (32)$$

$$\frac{dz}{dt}[0] = -v_0 \sin[\phi] \quad (33)$$

When solved these equations yield the terms

$$v_y[t] = \frac{E_{DC} - E_{DC} \cos \left[\frac{B_{RF} q_e t}{m_e} \right] + B_{RF} v_0 \cos \left[\frac{B_{RF} q_e t}{m_e} + \phi \right] - E_{RF} \left(+ \sin \left[\frac{B_{RF} q_e t}{m_e} \right] \right)}{B_{RF}} \quad (34)$$

$$v_z[t] = \frac{E_{RF} - E_{RF} \cos \left[\frac{B_{RF} q_e t}{m_e} \right] + E_{DC} \sin \left[\frac{B_{RF} q_e t}{m_e} \right] - B_{RF} v_0 \sin \left[\frac{B_{RF} q_e t}{m_e} + \phi \right]}{B_{RF}} \quad (35)$$

$$y[t] = \frac{1}{B_{RF}^2 q_e} B_{RF} \left(E_{DC} q_e t - 2m_e \sin \left[\frac{B_{RF} q_e t}{2m_e} \right] \left(E_{DC} \cos \left[\frac{B_{RF} q_e t}{2m_e} \right] - B_{RF} v_0 \cos \left[\frac{B_{RF} q_e t}{2m_e} + \phi \right] + E_{RF} \sin \left[\frac{B_{RF} q_e t}{2m_e} \right] \right) \right) \quad (36)$$

$$z[t] = \frac{1}{B_{RF}^2 q_e} \left(E_{DC} m_e - E_{DC} m_e \cos \left[\frac{B_{RF} q_e t}{m_e} \right] - B_{RF} m_e v_0 \cos[\phi] + B_{RF} m_e v_0 \cos \left[\frac{B_{RF} q_e t}{m_e} + \phi \right] + B_{RF} E_{RF} q_e t - E_{RF} m_e \sin \left[\frac{B_{RF} q_e t}{m_e} \right] \right) \quad (37)$$

The value for $z[t]$ may be numerically solved to get the particle transit time, which using the same process used to generate Equation 24 allows for the calculation of the energy associated with the particle at its time of impact with the dielectric window.

However, a further simplification of these equations is obtained when the magnetic field influence is negligible. In the limit of B_{RF} approaches zero, the equations of

motion indicated above simplify to the form of

$$v_y[t] = v_0 \cos[\phi] + \frac{q_e}{m_e} E_{RF} t \quad (38)$$

$$v_z[t] = -v_0 \sin[\phi] + \frac{q_e}{m_e} E_{DC} t \quad (39)$$

$$y[t] = v_0 \cos[\phi] t + \frac{1}{2} \frac{q_e}{m_e} E_{RF} t^2 \quad (40)$$

$$z[t] = -v_0 \sin[\phi] t + \frac{1}{2} \frac{q_e}{m_e} E_{DC} t^2 \quad (41)$$

Where the transit time τ is Equation 15. For a normal ejection ($\phi = \frac{\pi}{2}$) the final energy gained during the particle's flight is

$$\varepsilon_{Strike} = 2\varepsilon_{0m} + \frac{m_e \left(\frac{5}{4} E_{RF}^2 v_0^2 + \frac{1}{2} E_{DC}^2 v_0^2 + \frac{3}{4} E_{RF}^2 v_0^2 \right)}{(E_{DC})}. \quad (42)$$

After replacing the final calculation of the boundary curve equations and associating initial velocity with initial energy the E_{RF} field may be written as

$$E_{RF} = \left(\frac{4\sqrt{\varepsilon_{0m}(\varepsilon_{Strike} - \varepsilon_{0m})} - 2(\varepsilon_{Strike} - \varepsilon_{0m}) \sin[\psi]}{5\varepsilon_{0m} - \varepsilon_{Strike} + (3\varepsilon_{0m} + \varepsilon_{Strike}) \cos[\psi]} \right) E_{DC}. \quad (43)$$

showing the linear relationship that one would anticipate for the boundary curves in the static field case.

2.2 Method

As previously stated, when space charge effects are omitted modeled particles have no associated fields and when emitted from the dielectric do not have leave behind a positive charge and a bias field must be applied in the simulation in order to attract particles back to the surface of the dielectric enabling multipactor growth. In the NSC case, the simulation results may also be compared to analytic solutions for the boundary curves allowing for additional verification of computations run in ICEPIC.

Already both Fichtl [8] and Rogers [19] have had great successes in modeling lower boundary curves comparable to those of Kishek [14] and Lau [13].

Defining the EM Radiation.

Within the ICEPIC code, there is a capability to create a plane wave shape within the simulation space. This plane wave function allows for the simulation of electromagnetic radiation expected at the waveguide center. The plane wave modeled the electromagnetic radiation associated with a TE_{10} mode propagating approximately at the waveguide center. The electric field amplitude of the plane wave could be defined by the parameter `E0` and the frequency could be defined with the `frequency` parameter. A picture of the plane wave propagation through the dielectric may be seen in Figure 8. Note that PML's were used to prevent backscatter of the plane wave from the edges of the simulation. The plane wave shape defines the extent of the propagating electromagnetic radiation, a second dielectric was also used to prevent the back scatter of particles from interacting with the edges of the plane wave shape.

Particle Emission.

In order to define secondary particle emission special particle emissions must be defined to encompass any shape from which particle emission was desired. In order to understand the process of particle emission in ICEPIC, it becomes important to take a snap shot of the ICEPIC manual's definition of particle emission [5]. Since Fichtl and Rogers simulations [8] [19], the interactions between emitted `BEAM` and `SECONDARY` particle emission have been updated to classify secondary emission. The parameter `second_species_name` defines the species with which a particular particle region interacts. This improvement results in three different particle shapes being

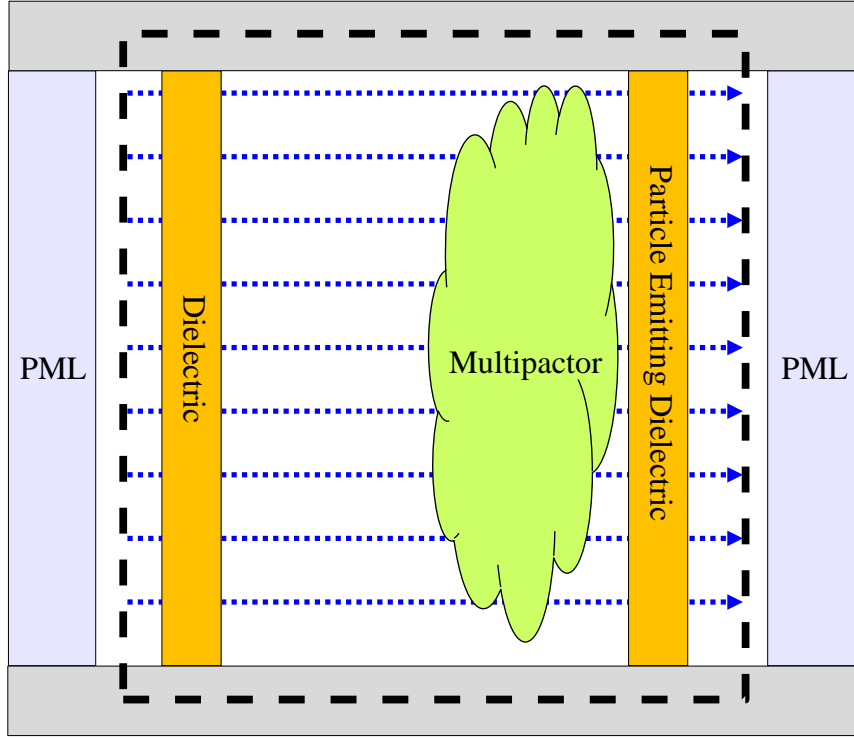


Figure 8. The plane wave shape defined within the ICEPIC environment along with the expected region of multipactor within the system setup.

used to define primary emitted particles, the secondary emitting region that reacts to the presence of primary particles, and a secondary emitting region that reacts to secondary particles emitted. In the ICEPIC code, the primary emitted particles are defined by direction injection, the rate of injection and their average temperatures.

Secondary emission shapes have a few different properties than that associated with primary emission regions. They follow the empirical equations of secondary electron emission developed by Vaughan [24]. Material parameters out of these equations are used to define secondary emission from this particle shape, as well as scattering and reflection coefficients dealing with the material's interaction with the impacting particles. The parameters used for the mapping of the boundary curves followed from values used by Fichtl, Rogers, and Kishek [8] [19] [15] and are reproduced in Table 1.

Table 1. Parameters from Fichtl [8] used to verify ICEPIC simulation setup, and in remapping the susceptibility diagrams.

δ_{max0}	2
\mathcal{E}_{max0}	400 eV
k_s	1
T	2.1 eV
<i>Resolution</i>	3000

Static Field Implementation.

For the NSC case, a bias field is required to return particles to the surface within the simulation. Within the simulation environment static uniform electric fields are able to be defined for the entire simulation environment with the `default_e` command. Uniform magnetic fields may also be assigned to the environment with the `default_b` command. By applying static electric field within the simulation in the $-\hat{z}$ direction, the bias field associated with the NSC mapping may be achieved.

Building Susceptibility Curves.

By parametrically varying the values for the plane wave field amplitude and the bias electric field, the susceptibility diagram was constructed. As seen in Figure 9 and Figure 10, the construction of the boundary curves involved mapping the outcome, growth or decay, resulting from a survey of E_{\parallel} values for a single fixed value of the bias electric field, E_{\perp} . This was then repeated for a sequence of new bias electric field inputs. The resulting points differentiating growth and decay regions were then fitted with a linear regression corresponding to the linear relationship observed in Equation 25. The slopes were then recorded and compared to theory.

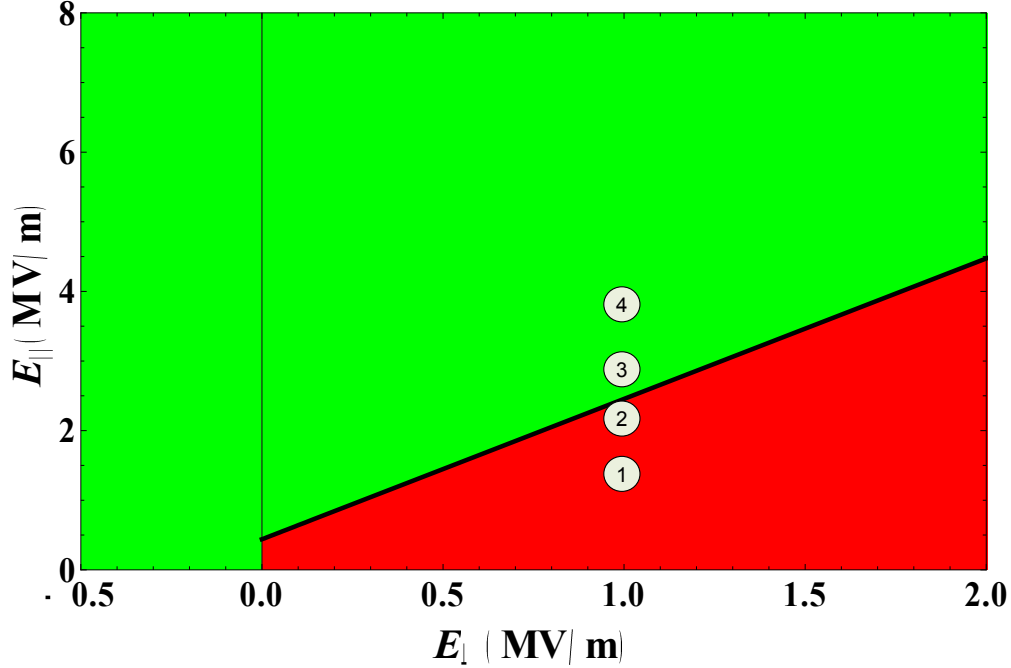
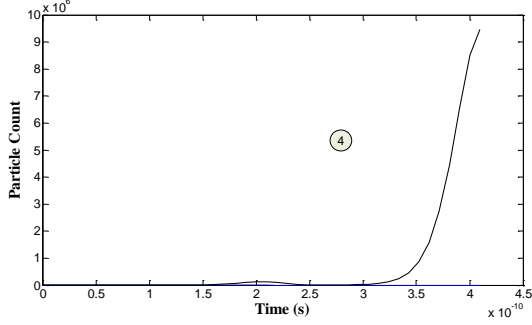


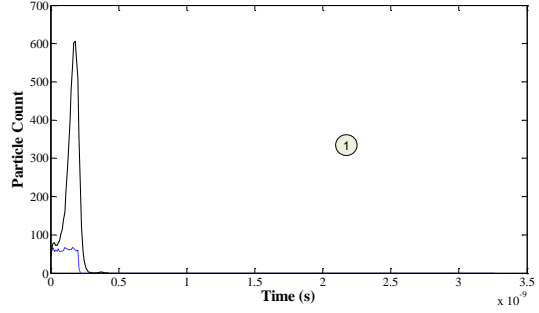
Figure 9. Boundary curve generated from observing the growth and decay of multiplier by parametrically surveying E_{\perp} and E_{\parallel} for given parameters. The numbers in bubbles correspond to growth and decay particle populations represented in Figure 10.

2.3 Results and Analysis

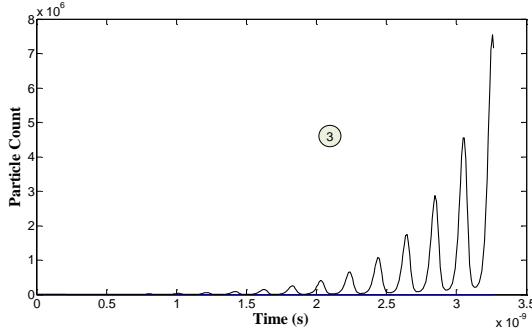
Previous results in characterizing boundary curves in the susceptibility diagram were reported by Kishek and Lau [15]. These follow the linear boundary conditions indicated in Figure 11, which confirmed the results previously indicated for the theoretical boundary curve indicated in Equation 25. In Fichtl’s and Roger’s work only the lower boundary curve was analyzed to confirm the validity of ICEPIC measurements [8] [19]. However when the boundary curve associated with the high crossover energy (ε_2) was analyzed in ICEPIC, a large discrepancy was observed between the remapping and previous results from Monte Carlo and other PIC code simulations [3] [13] [15] [22] [12]. The new susceptibility mapping is shown in Figure 12. After examining the simulation, the source of this discrepancy was traced to the use of the plane wave feature in ICEPIC. In previous techniques for mapping susceptibility di-



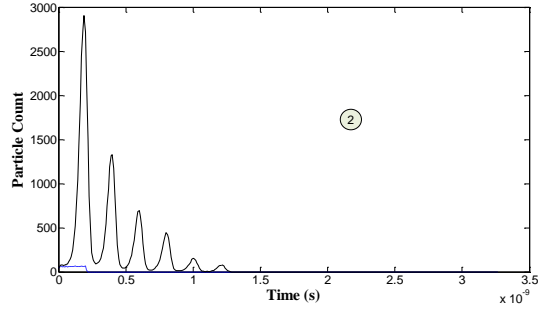
(a) Well above boundary curve at with field values of $E_{\parallel} = 3.3MV/m$ and $E_{\perp} = 1MV/m$



(b) Well below boundary curve at with field values of $E_{\parallel} = 1.8MV/m$ and $E_{\perp} = 1MV/m$



(c) Just above boundary curve at with field values of $E_{\parallel} = 2.5MV/m$ and $E_{\perp} = 1MV/m$



(d) Just below boundary curve at with field values of $E_{\parallel} = 2.3MV/m$ and $E_{\perp} = 1MV/m$

Figure 10. A temporal variation of total particle population in the vicinity of growth and decay around the boundary curve. The numbers in the bubbles correspond to the numbers in Figure 9 showing the process to create a susceptibility diagram.

agrams, Monte Carlo techniques have only considered the electric field component of electromagnetic radiation propagating through the waveguide dielectric. In contrast, the plane wave shape in ICEPIC also contains the magnetic field component present in the radiation propagating through the dielectric.

In order to confirm the magnetic field as the origin of the discrepancy, another mapping was accomplished using static electric and magnetic fields to represent the incoming EM radiation. These results did confirm the origin of the shift of the curve associated with higher energy, ε_2 , boundary. This shift is shown in Figure 13, where the change in the slope of the boundary curve associate with ε_2 is apparent.

To summarize, the lower boundary curve associated with the first crossover energy

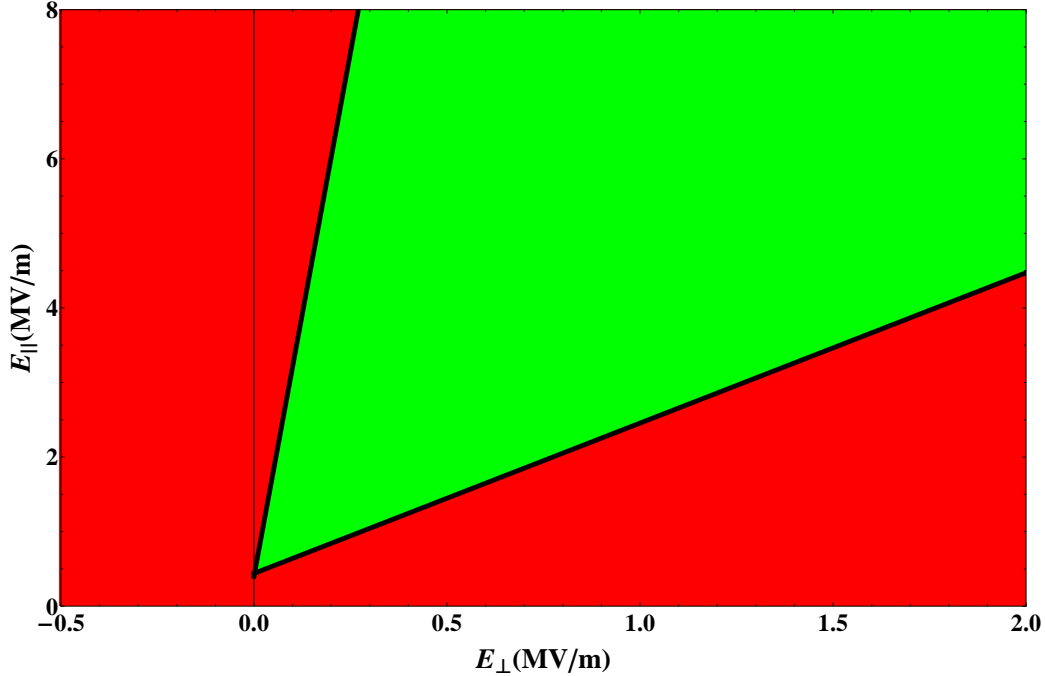


Figure 11. Recreation of previous work by Kishek and Lau [15]. The boundary curves have been fitted with a linear regression to capture their extent.

ε_1 , tends to follow closely with previous work done on analyzing the boundary curves. The slope of this first crossover energy is slightly higher in the E_{static} case. However, in the case of the upper boundary curve associated with the impact energy ε_2 the slope comparison confirms that the magnetic field causes multipactor growth at high enough E_{\parallel} values despite the presence of no return field, $E_{\perp} = 0$.

These differences in slope change between the upper and lower boundary curves can be clarified by considering the Lorentz force imparted by the magnetic field. By again using the linear slope analogy, Equation 25 and Equation 43 lead to the form of the boundary curve

$$E_{\parallel} = \gamma E_{\perp eff} \quad (44)$$

where γ is defined as the slope of the boundary curve produced with consideration of only the electric field and $E_{\perp eff}$ is the effective electric field. By defining $E_{\perp eff}$ as a function of the magnetic and electric field for a particle with an average velocity

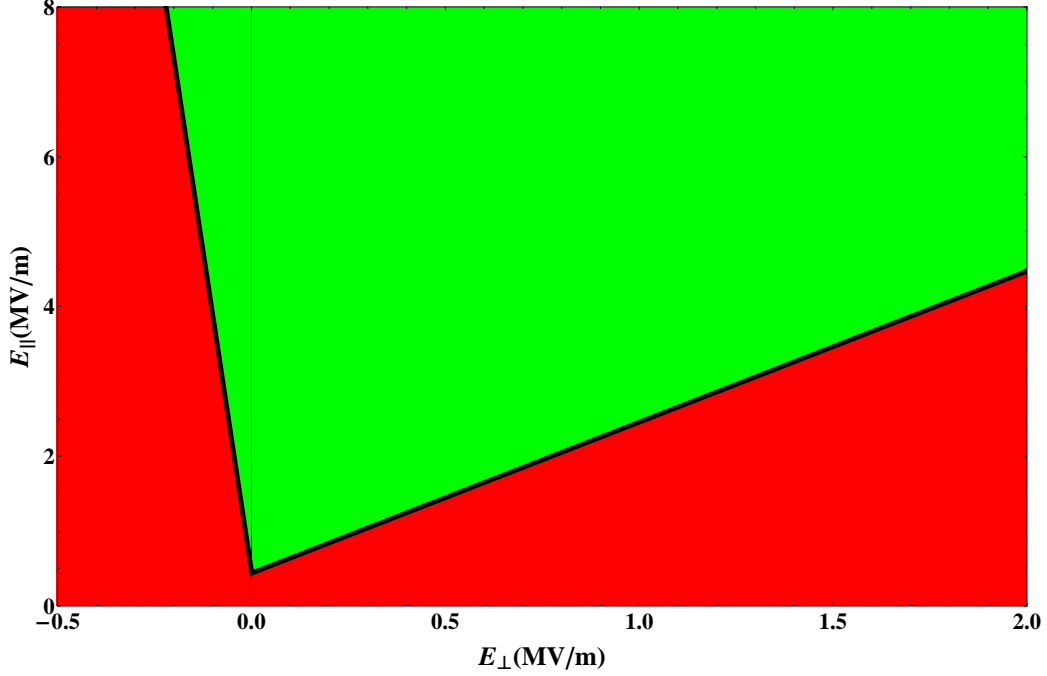


Figure 12. Susceptibility diagram results based on the ICEPIC outputs using the plane wave shape command. Includes both a dynamically varying E_{\parallel} and B_{\parallel} fields.

$\langle v_{avg} \rangle$ for the length of transit leads to the equation

$$E_{\parallel} = \gamma(E_{DC} + \langle v \rangle_{avg} B_{\parallel}) \quad (45)$$

and considering $B_{\parallel} = \frac{E_{\parallel}}{c}$, obtain

$$\begin{aligned} E_{\parallel} &= \gamma(E_{DC} + \frac{\langle v \rangle_{avg}}{c} E_{\parallel}) \\ E_{\parallel} &= \frac{\gamma E_{DC}}{(1 - \gamma \frac{\langle v \rangle_{avg}}{c})} \end{aligned} \quad (46)$$

which we may relabel as a new effective slope γ_{Bfield} to form

$$E_{\parallel} = \gamma_{Bfield} E_{DC} \quad (47)$$

where

$$\gamma_{Bfield} = \frac{\gamma}{(1 - \gamma \frac{\langle v \rangle_{avg}}{c})}$$

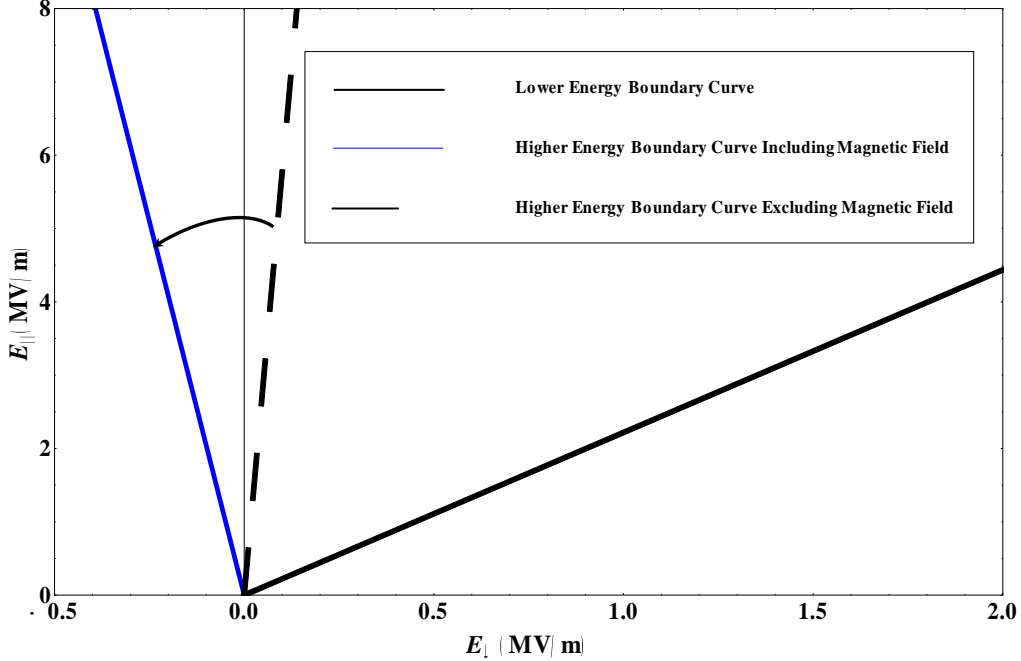


Figure 13. The results of mapping the boundary curves for the static field case. Note the shift that occurs when a magnetic field whose amplitude is equivalent to the amplitude of a magnetic field in a plane wave ($B_{\parallel} = \frac{E_{\parallel}}{c}$).

This equation establishes the shift in the curves based on the inclusion of the magnetic field and leads to the results pictured in Figure 14. As one can see, there is very close agreement to the expected shift actually observed in the remapping of the magnetic field into a new form. A summary of linear regression results are presented in Table 2.

The remapped susceptibility diagram indicates an opportunity to mitigate the initiation of multipactor with the application of an external bias field. From Figure 12,

Table 2. Summary of linear regressions for boundary curves illustrated in figures 11, 12, 13. The values are organized by their association with the lower (ε_1) and higher (ε_2) cutoff energies associated with electron impact.

Study	Boundary Curve ε_1		Boundary Curve ε_2	
	Slope	Intercept	Slope	Intercept
Original Kishek [15]	1.54	0.1	28.1	1.2
Planewave	2.01	0.43	-34.2	0.48
E_{static}	2.22	-0.03	57.67	0.10
E_{static} and B_{static}	2.25	-0.04	-20.39	-.53

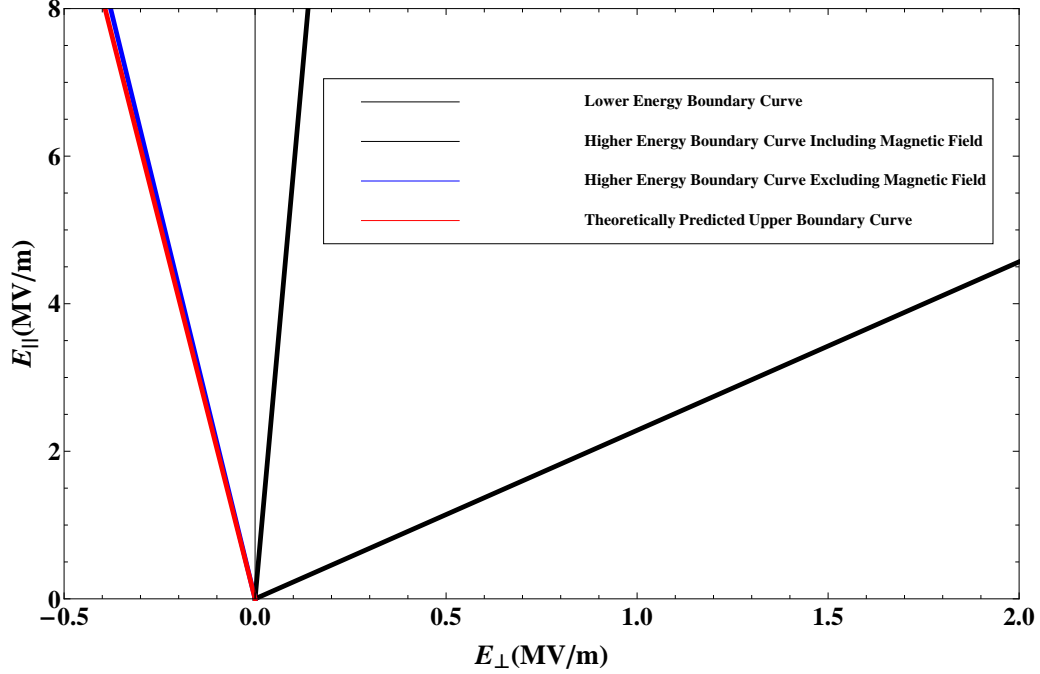


Figure 14. Theoretical line fitting of the shifted upper boundary in the static field based upon Equation 47 showing agreement between in the shift observed with the theoretical model including the magnetic Lorentz force.

the required bias to prevent secondary emission growth is much less if it is applied in the $-\hat{z}$ direction in respect to the simulation setup. This has been previously indicated in Spaulding’s work in characterizing the application of an external bias field in preventing the growth of multipactor [21] and is confirmed in the new susceptibility mapping.

III. Analysis and Simulation of Reflection

The multipactor mitigation problem stems from the conventional properties of a plasma's interaction with high intensity electromagnetic energy at microwave frequencies. These frequencies typically range from 1–3 *GHz* and tend to lead the electron cascade process at 1–3 *MV/m* electric field intensities. At these levels the plasma will begin to exhibit some interesting effects, primarily the reflection of microwave radiation at the dielectric window and the heating of the dielectric window. In this chapter, the reflection associated with multipactor plasma is characterized with both analytic development and simulation. In order to properly characterize the electron cloud formed along the dielectric, the Space Charge must be included in the particle's interaction with the electromagnetic field and with each other.

3.1 Theory

Understanding Multipactor in Real Time.

In the SC case, the incoming microwave radiation is in the form of a $TE_{1,0}$ mode propagating inside the waveguide before propagating through the dielectric surface. Previous experiments completed by Neuber at Texas Tech [16] indicate that the region most prone to multipactor is along the center of the waveguide window corresponding to the greatest values for E_{\parallel} in the $TE_{1,0}$ mode. In this region of the electromagnetic mode, the microwave radiation may be approximated with as a plane wave normally incident on the dielectric window.

An example of particle growth associated with the space charge case is shown in Figure 15. It illustrates that the particle growth follows a linearly increasing oscillation, with the frequency of oscillation in particle numbers corresponding to twice the frequency of the propagating electromagnetic radiation. In the SC case, particles are

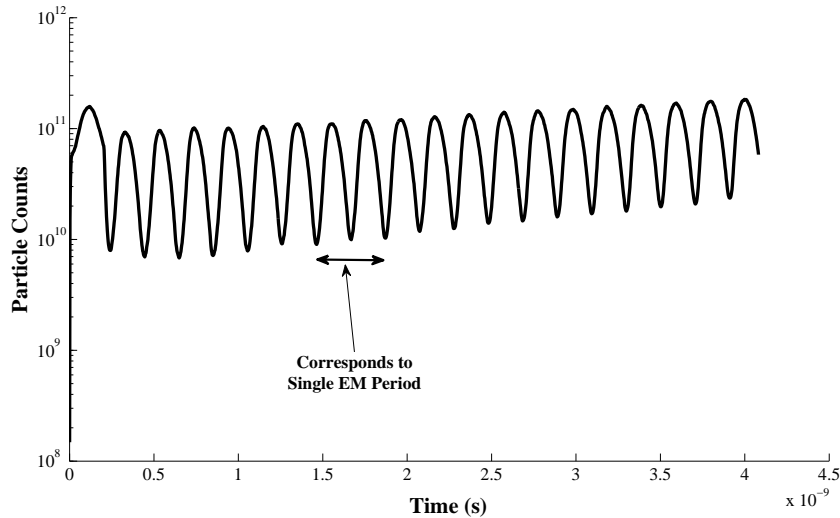


Figure 15. The dynamic particle growth associated in a multipacting system. The propagating electromagnetic energy causing the particle growth has a field amplitude of $E_{\parallel} = 3MV/m$ and a frequency of $f = 2.45GHz$. Every two periods of particle oscillation corresponds to a single period of the microwave radiation.

returned to the surface of the dielectric primarily by compensating positive surface charge left on emitting surface. By parametrically plotting the E_{\parallel} field associated with the plane wave and the E_{\perp} field associated with the surface charge oscillation, a “bowtie” curve is constructed. The “bowtie” curve is a valuable tool in characterizing the temporal variation of multipactor.

By following the arrows in the “bowtie” curve plotted in Figure 16, the evolution of secondary particle emission begins with the E_{\parallel} field supplying energy to shift the average impact energy of electrons into a region of multipactor initiation. These particles continue to impact with the surface causing an electron avalanche that leads to an increasing E_{\perp} field. Eventually, the E_{\parallel} field begins to decrease corresponding with the sinusoidal oscillation of the plane wave propagating through the dielectric. This leads to lowering the average impact energy of particles in the electron cloud. Eventually, the average impact energy falls below the boundary curve, leading to multipactor decay and a consequent decrease in the number of particles present in the electron cloud. This process is then repeated for negative values of the E_{\parallel} field, indicating that

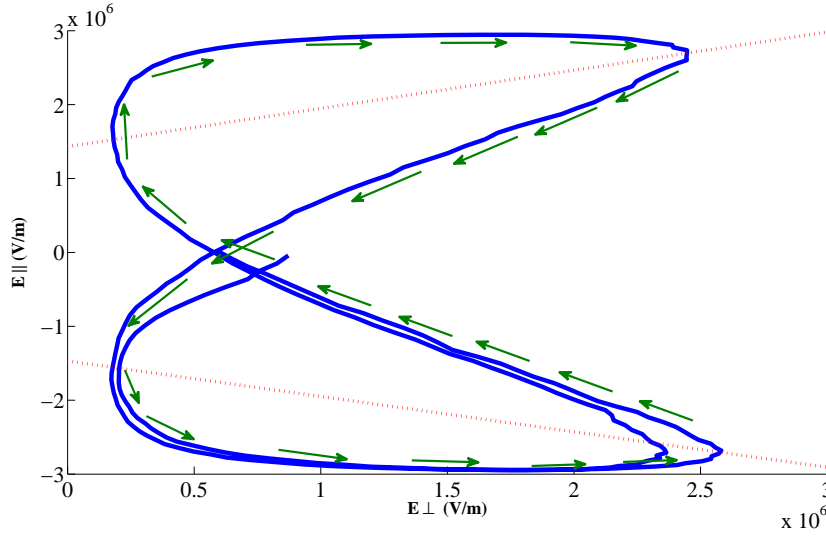


Figure 16. “Bowtie” curves based on Kim and Verboncoeur’s previous work [12] in characterizing multipactor growth and decay. This curve represents the steady state dynamics of the E_{\parallel} and E_{\perp} fields parametrically plotted in relation to each other. The red lines correspond to boundary curves associated with separating regions of multipactor growth and decay. The arrows shows the direction that the fields evolve

only the field amplitude is important in determining multipactor growth and decay. It is important to understand this evolution of particle count when characterizing the reflection of electromagnetic radiation.

Calculating the Power Transmitted through the Multipactor.

The reflection problem of microwave radiation stems from the underlying issues concerning all plasmas reaction with electromagnetic radiation. As seen in Fox’s textbook [9], the theory behind bulk plasmon effects in materials could be applied to

the microwave multipactor problem. Starting with Maxwell's equations

$$\nabla \cdot \vec{E} = \frac{\rho}{\epsilon_0} \quad (48)$$

$$\nabla \cdot \vec{B} = 0 \quad (49)$$

$$\nabla \times \vec{E} = -\frac{\partial \vec{B}}{\partial t} \quad (50)$$

$$\vec{j} + \epsilon_0 \frac{\partial \vec{E}}{\partial t} = \frac{1}{\mu_0} \nabla \times \vec{B}. \quad (51)$$

one may develop the wave equation for electromagnetic radiation by taking the derivative of equation 51 and substituting Equation 50 [9]

$$\frac{\partial \vec{j}}{\partial t} + \epsilon_0 \frac{\partial^2 \vec{E}}{\partial t^2} = -\frac{1}{\mu_0} \nabla \times (\nabla \times \vec{E}). \quad (52)$$

The electrons will move according to the electric field $m_e \ddot{v} = -q_e \vec{E}$ and current may be expressed as $\vec{j} = -n_e q_e \vec{v}$. Using these two equations allows one to write the change in current density as $\frac{\partial \vec{j}}{\partial t} = \frac{n_e q_e^2}{\epsilon_0 m_e} \vec{E}$. Substituting this and $c^2 = \frac{1}{\epsilon_0 \mu_0}$ into Equation 52 reveals:

$$\frac{\partial^2 \vec{E}}{\partial t^2} + \left(\frac{n_e q_e^2}{\epsilon_0 m_e}\right) \vec{E} = -c^2 \nabla \times (\nabla \times \vec{E}) \quad (53)$$

where $\frac{n_e q_e^2}{\epsilon_0 m_e}$ is normally identified the plasma frequency:

$$\omega_p^2 = \frac{N_e q_e^2}{\epsilon_0 m_e}. \quad (54)$$

Knowing that the electric field may be split into its transverse and longitudinal components allows one to write equation 53 as two independent field equations:

$$\frac{\partial^2 \vec{E}_t}{\partial t^2} + \omega_p^2 \vec{E}_t - c^2 \nabla^2 \vec{E}_t = 0 \quad (55)$$

and

$$\frac{\partial^2 \vec{E}_l}{\partial t^2} + \omega_p^2 \vec{E}_l = 0. \quad (56)$$

Assuming a plane wave solution for Equation 55 the electric field of the traveling wave is

$$E_{\parallel} = E_0 e^{i(\vec{k} \cdot \vec{r} - \omega t)} \quad (57)$$

where the relation between \vec{k} and ω is

$$c^2 |\vec{k}|^2 = \omega^2 - \omega_p^2. \quad (58)$$

Observe that radiation with an angular frequency less than the plasma frequency will not propagate through the extent of the plasma [9]. With minor rewriting of Equation 58 the refractive index for the plasma may then be found.

$$n^2 = 1 - \frac{\omega_p^2}{\omega^2}. \quad (59)$$

Assuming propagation in the \hat{z} -direction and writing k in terms of the refractive index n , we obtain a new form of Equation 57

$$E_{\parallel} = E_0 e^{i(k_z z - \omega t)} = E_0 e^{i\left(\frac{n\omega}{c} z - \omega t\right)} = E_0 e^{i\left(\frac{\left(\sqrt{\omega^2 - \omega_p^2}\right)}{c} z - \omega t\right)}. \quad (60)$$

Notice that if the refractive index and the wave vector become pure imaginary, the field amplitude will decay exponentially. This will occur if

$$\omega_p > \omega. \quad (61)$$

The transverse field solution shown in Equation 60 may then be rewritten as

$$E_{\parallel} = E_0 e^{-\int \alpha(z) dz} e^{-i\omega t} \quad (62)$$

where

$$\alpha(z) = \frac{\left(\sqrt{\omega_p(z)^2 - \omega^2}\right)}{c}. \quad (63)$$

By using Valfell's [22] particle density distribution characterizing the extent of the multipactor cloud,

$$n(z) = \frac{n_0}{\left(1 + \frac{\omega_p z}{v_t}\right)^2} \quad (64)$$

where

$$v_t = \sqrt{\frac{2\varepsilon_0}{m_e}}$$

and

$$\omega_p = \sqrt{\frac{n_0 q_e^2}{m_e \varepsilon_0}}, \quad (65)$$

Equation 63 may be rewritten as

$$\alpha(z) = \frac{\left(\sqrt{1 - \left(\frac{\omega}{\omega_p} + \frac{\omega z}{v_t}\right)^2}\right)}{\lambda_0 \left(\frac{\omega}{\omega_p} + \frac{\omega z}{v_t}\right)}. \quad (66)$$

This can be further simplified by writing

$$\alpha(z) = \frac{1}{\lambda_0} \frac{\left(\sqrt{1 - \beta(z)^2}\right)}{\beta(z)}, \quad (67)$$

where

$$\beta(z) = \frac{\omega}{\omega_p} + \frac{\omega z}{v_t}.$$

Integrating $\int \alpha(z) dz$ over the range of the multipactor extent leads to

$$\begin{aligned}
\int \alpha(z) dz &= \int \alpha(\beta) \frac{dz}{d\beta} d\beta = \frac{v_t}{\omega} \int \alpha(\beta) d\beta \\
&= \frac{v_t}{c} \int_{\frac{\omega}{\omega_p}=\xi}^1 \frac{\left(\sqrt{1-\beta^2}\right)}{\beta} d\beta \\
&= -\frac{v_t}{c} \left(-\sqrt{1-\xi^2} - \text{Ln}[\xi] + \text{Ln} \left[1 + \sqrt{1-\xi^2} \right] \right). \quad (68)
\end{aligned}$$

Equation 68 leads to a wave equation for the electric field transmitted through the full extent of the multipactor plasma

$$\begin{aligned}
\psi &= E_0 e^{-\frac{v_t}{c} \left(-\sqrt{1-\xi^2} - \text{Ln}[\xi] + \text{Ln} \left[1 + \sqrt{1-\xi^2} \right] \right)} e^{-i\omega t} \\
&= E_0 e^{\frac{v_t}{c} \left(\sqrt{1-\xi^2} + \text{Ln}[\xi] - \text{Ln} \left[1 + \sqrt{1-\xi^2} \right] \right)} e^{-i\omega t} \quad (69)
\end{aligned}$$

Knowing that the intensity of the microwave radiation related to the electric field is a function of the Poynting vector [10]

$$|\vec{S}| = \epsilon_0 c \psi^2, \quad (70)$$

allows for Equation 69 to be rewritten as a function of intensity

$$|\vec{S}_{Trans}| = \epsilon_0 c E_0^2 e^{2\frac{v_t}{c} \left(\sqrt{1-\xi^2} + \text{Ln}[\xi] - \text{Ln} \left[1 + \sqrt{1-\xi^2} \right] \right)}. \quad (71)$$

Equation 71 may be then converted to the transmitted power by multiplying the intensity by the area of the plane wave

$$\begin{aligned}
P_{Transmitted} &= (\Delta x \Delta y) \epsilon_0 c E_0^2 e^{2\frac{v_t}{c} (\sqrt{1-\xi^2} + \text{Ln}[\xi] - \text{Ln}[1 + \sqrt{1-\xi^2}])} \\
&= (\Delta x \Delta y) \epsilon_0 c E_0^2 \left(\frac{\xi}{1 + \sqrt{1-\xi^2}} \right)^{\frac{2v_t}{c}} e^{\frac{2v_t}{c} \sqrt{1-\xi^2}} \quad (72)
\end{aligned}$$

where

$$\xi = \frac{\omega}{\omega_p}.$$

Rewriting Equation 72 as a new function of $\frac{\omega_p}{\omega}$

$$T = \left(\frac{\left(\frac{1}{\kappa}\right)}{1 + \sqrt{1 - \left(\frac{1}{\kappa}\right)^2}} \right)^{\frac{2v_t}{c}} e^{\frac{2v_t}{c} \sqrt{1 - \left(\frac{1}{\kappa}\right)^2}} \quad (73)$$

where

$$\kappa = \frac{\omega_p}{\omega}.$$

Figure 17 illustrates the curve relating the transmission coefficient to the ratio of the plasma frequency to the angular frequency of the propagating electromagnetic radiation. The transmission coefficient is based on the angular frequency of the propagating EM radiation (ω), the emitted electron velocity that is dependent upon material constituting the dielectric (v_t), and the plasma frequency based upon the particle density at the dielectric surface (ω_p). The only value reliant on the electric field amplitude of the propagating microwave radiation is going to be the plasma frequency due to its dependence on the particle density. As particle count increases the transmission of radiation decreases through the multipactor. If the particle density becomes great enough, there will be no transmission through the multipactor approaching the limiting case of a total plasma reflection associated with plasmas where the plasma extent is much larger than the wavelength of the propagating elec-

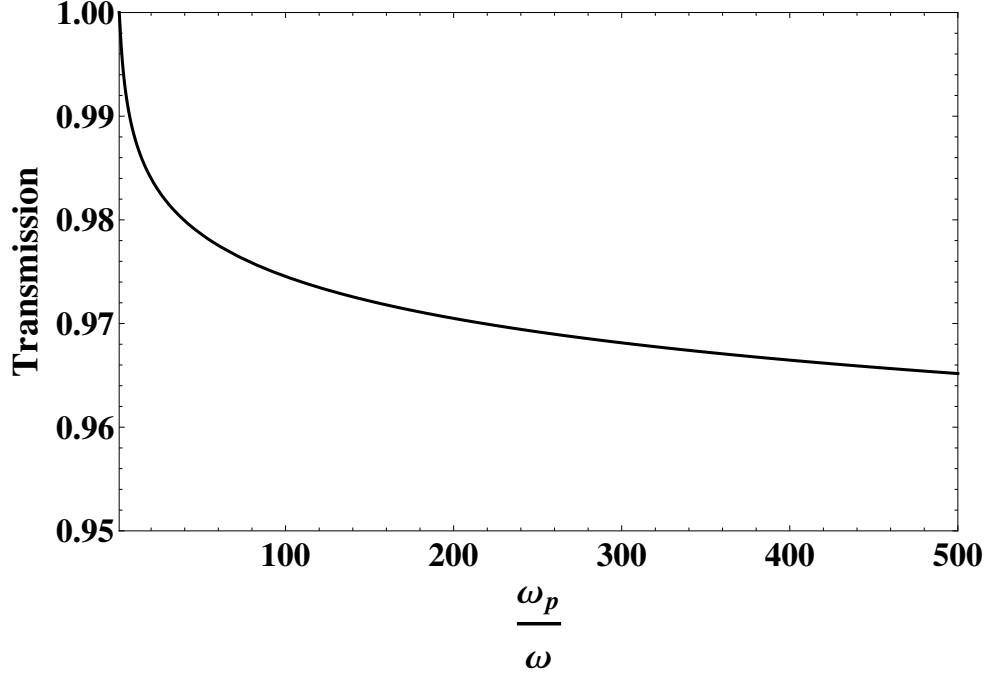


Figure 17. The curve relating transmission coefficient to the ratio of the plasma frequency (ω_p) to the angular frequency ω of the plane wave propagating through the multipactor generated from Equation 73. The electron velocity (v_t) corresponds to an electron emitted with an energy of $\varepsilon_0 = 2eV$.

tromagnetic radiation.

Calculating the Intensity Reflected.

In order to calculate the power per unit area reflected for microwave radiation incident on the dielectric surface, one may relate Equation 72 to the incident plane wave intensity by

$$P_{Reflected} = P_{Incident} - (P_{Deposited} + P_{Transmitted}). \quad (74)$$

In which $P_{Deposited}$ is defined by Valfells [22] to be

$$P_{Deposited} = \frac{\sqrt{\pi}}{4} \left[2 < \varepsilon_0 > \frac{m_e \varepsilon_0}{q_e^2} \omega_p^2 v_t + \varepsilon_0 v_t E_{\parallel}^2 \left(\frac{\omega_p}{\omega} \right)^2 G \left(\frac{\omega_p}{\omega} \right) \right], \quad (75)$$

where

$$G \left(\frac{\omega}{\omega_p} \right) = 1 - 2 \frac{2\sqrt{2}}{\sqrt{\pi}} \int_0^{\infty} \cos \left[\sqrt{2\pi} \frac{\omega \exp(y^2) \operatorname{erf}(y)}{\omega_p} \right] \exp(-2y^2) dy \quad (76)$$

with this final equation the reflected power may be calculated analytically from Valfell's equation for power deposition and the new equation developed for the intensity of the electromagnetic radiation transmitted through the multipactor.

In order to relate the transmitted power in Equation 72 and the power deposited from Equation 75 to the number of particles indicated in the ICEPIC output files, the charge density at the surface of the dielectric, n_0 , had to be related to the total charge contained in the multipactor cloud N_{Tot} . This may be accomplished by expressing N_{Tot} as a function of n_0 using Valfell's charge distribution [22]

$$\begin{aligned}
 N_{\text{Tot}} &= \int_0^\infty \int_0^{\Delta y} \int_0^{\Delta x} \frac{n_0}{\left(1 + \frac{\omega_p z}{v_t}\right)^2} dx dy dz = n_0 * \frac{v_t}{\omega_p} \Delta x \Delta y \\
 &= v_t \frac{n_0}{\sqrt{\frac{n_0 q_e^2}{m_e \epsilon_0}}} \Delta x \Delta y = v_t \sqrt{\frac{n_0 m_e \epsilon_0}{q_e^2}} \Delta x \Delta y. \tag{77}
 \end{aligned}$$

With this derived relationship the total power transmitted through the multipactor may be calculated from the total amount of particles in the multipactor (N_{Tot}).

3.2 Methodology

Reflection of the Dielectric Window.

Before quantifying the reflection of multipactor within the cavity, the reflection associated with the dielectric window must be considered in order to properly identify reflection associated with the dielectric and reflection associated with the multipactor. Within ICEPIC, the dielectric constant of the windows is set to be ϵ_{Window} to 1.0001, resembling the dielectric constant associated with anti-reflection coatings present on current window dielectrics used in HPM devices[4]. The actual reflection coefficient

is calculated to be

$$R = \left| \frac{n-1}{n+1} \right|^2 \approx \left| \frac{\sqrt{\epsilon}-1}{\sqrt{\epsilon}+1} \right|^2 = 6.24 \times 10^{-10}, \quad (78)$$

indicating that the reflection at the dielectric windows for the simulated value of ϵ is negligible in comparison to the reflection value of the multipactor found by Fichtl [8], justifying it being ignored within this analysis.

Using PROBE to Determine Electric Fields.

The determination of electric fields associated with reflection and transmission was completed using the PROBE dump command in ICEPIC. This was a useful tool in analyzing the electric field at specific points within the simulation. Each selected z location was given seven (matching N_x) uniformly spaced PROBE dumps creating a probe line which when averaged allows for the elimination of noise in the analysis of the electric and magnetic fields. Locations of these probe lines are illustrated in Figure 18. Probe lines were chosen primarily to analyze two different parts of the system, the reflection of the planar wave and the parallel and perpendicular electric fields associated with the system, E_{Ref} measures the electric field amplitude reflected from the particle cloud in front of the dielectric window, E_{Trans} corresponds to the field transmitted through the particle cloud, E_{Inc} is used to measure the field initially launched by the [Planewave] section of the code, and E_{DC} is used to measure fields perpendicular and parallel to the surface of the dielectric. However, the E_{Inc} probe will contain a superposition of the reflected and incident waves. as shown in equation

$$\vec{E}_{Inc} = \vec{E}_{Orig} + \vec{E}_{Ref} \quad (79)$$

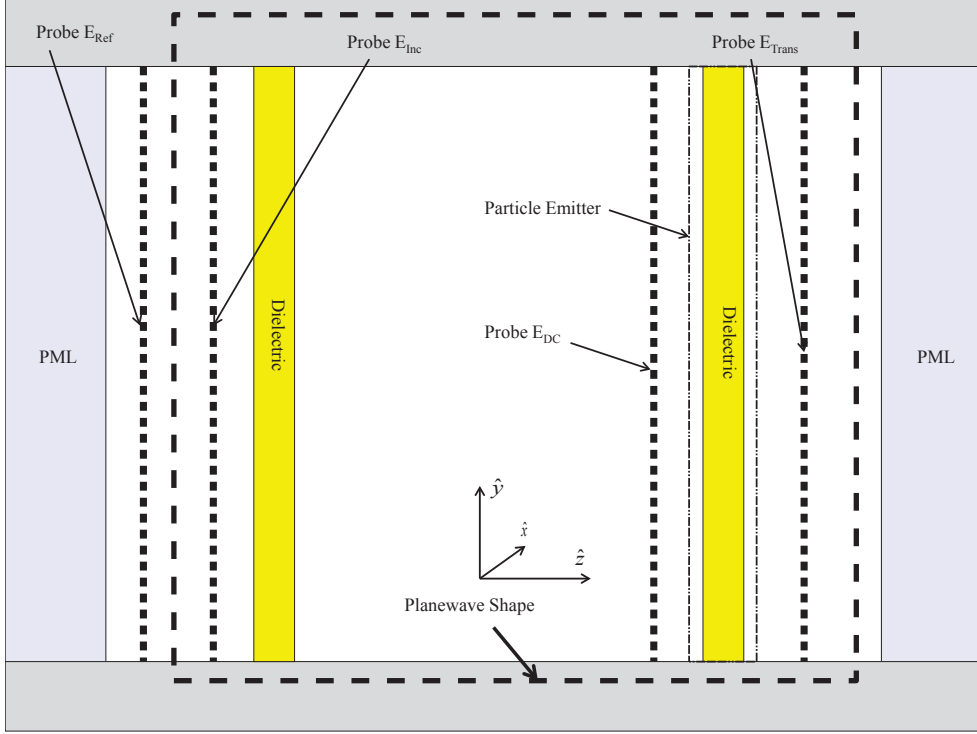


Figure 18. Various “probe line” locations within the simulation. They indicate the position of the probes measuring E_{Ref} to be in a place that will receive only the reflected EM radiation generated by the plane wave. The probes measuring E_{Inc} measure the initial generated electric field. Probe E_{DC} measures the electric fields close to the dielectric to ascertain the relationship between E_{\perp} and E_{\parallel} . The probes known as E_{Trans} measure the EM radiation transmitted through the dielectric.

where E_{Orig} is the original emitted electric field. As indicated by equation 78 there will be very little reflection from the dielectric windows in the model. Therefore, within the simulation reflected electromagnetic energy will be primarily attributed to the multipactor on the outside of the dielectric window. The rest of the material properties, were based on Verboncoeurs [12] and Rogers [19] previous work for characterizing secondary electron emission contained in Table 3. With this knowledge of field oscillations received from the PROBE dump, a simple calculation [10] using

$$\langle S \rangle = \frac{\epsilon c}{2} \langle E \rangle^2 \quad (80)$$

$$\langle P \rangle = \langle S \rangle x_{sys} y_{sys} \quad (81)$$

Table 3. Parameters from Rogers [19] used to verify ICEPIC simulation setup.

δ_{max0}	3
\mathcal{E}_{max0}	420 eV
k_s	1
T	2.1 eV
<i>Resolution</i>	12000

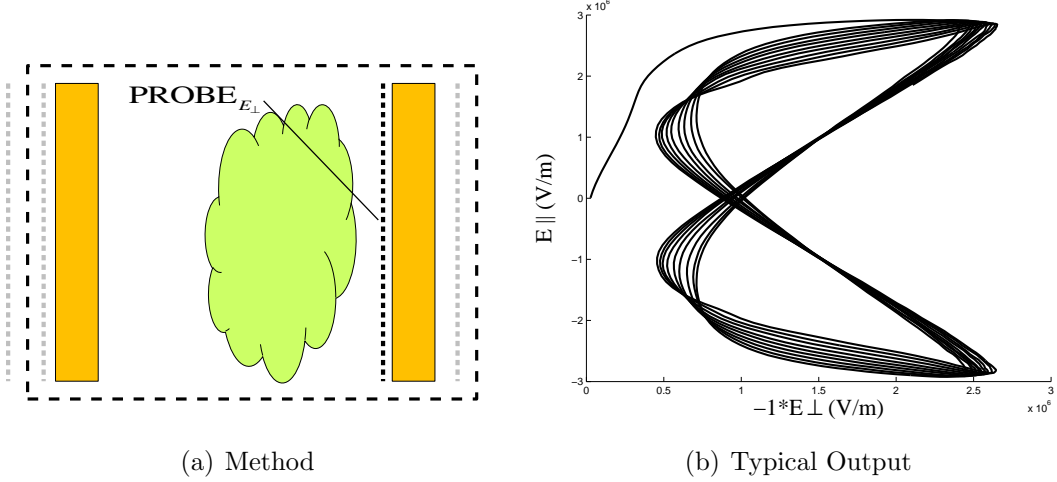


Figure 19. Using the results from the Probe E_{DC} to manufacture the “Bowtie” curves associated with varying electric fields for an electric field amplitude of $E_{\parallel} = 3MV/m$ and $f = 2.45GHz$.

where x_{sys} and y_{sys} are the respective dimensions of the simulation in the \hat{x} and \hat{y} directions enables the calculation of power being transmitted as a function of the electric field in the system. As indicated in Section 3.1 the “bowtie” curves are excellent tools in determining the characteristics associated with the temporal variation of the multipactor plasma. By measuring both the E_{\perp} and E_{\parallel} fields with the probe E_{DC} line, the parametric relationship between both E_{\parallel} and E_{\perp} may be plotted as shown in Figure 19.

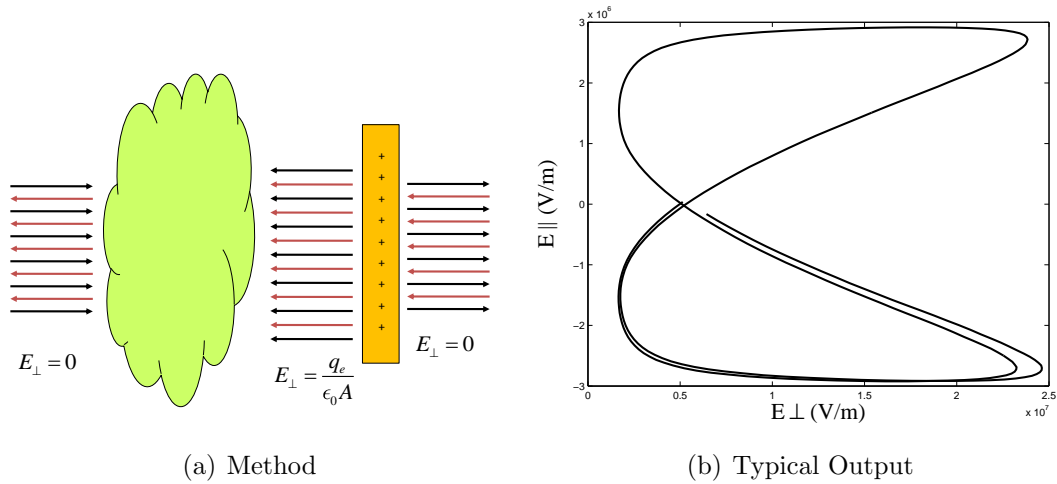


Figure 20. Using Equation 82 to derive the E_{\perp} field based on the particle count and weight present in the multipactor cloud.

Using Particle Count to Determine Electric Field Perpendicular.

The benefit of knowing the particle count in the space charge case comes from the ability to calculate the E_{\perp} field from the charged particles. If we treat the sheet of positive charge on the dielectric as being a surface charge, and also treat the electric field produced by the electrons in the same manner, the superposition of the electric fields leads to the equation

$$\vec{E} = \frac{Q_{Tot}}{\epsilon_0 A} \quad (82)$$

where Q_{Tot} is defined as the total charge associated with the window dielectric and A is the area of the simulation space in the x-y plane. A “bowtie” trajectory constructed of using the particle count to generate the E_{\perp} field is displayed in Figure 20. This technique also removes the noise associated with the method of using the probe E_{DC} line measurements pictured in Figure 19. The methods show that there is a discrepancy that exists between the values reported by both methods.

Particle Weighting.

Due to the requirement for computational efficiency, the ICEPIC code does not treat electrons as single particles in the system. Rather, numbers of electrons are grouped together into single pseudoparticles. It is therefore necessary to establish the total charge available in the multipactor cloud within an accurate particle weighting to relate the number of macroparticles in the ICEPIC code to the number of electrons being represented by each macroparticle. This becomes important for the calculation of both the reflection and the evaluation of the E_{\perp} field.

The particle weighting is initially determined in the simulation based on the beam parameters associated with the initial current injected in the simulation to initiate multipactor. The calculation of this weighting is based upon the the charge associated with the macroparticle [5]

$$q_{macro} = \frac{\text{current inject_interval dt}}{\text{inject}} \frac{A_{Cell}}{A_{Emission}} \quad (83)$$

which combined with

$$\text{weight} = \frac{q_{macro}}{q_e}. \quad (84)$$

Definition of these quantities used in Equation 83 are

- **current** - This dictates an overall current (in *Amps*) maintained by the emitting surface. This plays into the weighting the weighting of particles by dictating a required charge per shape injected into the system.
- **inject** - This is the amount of particles injected from each cell of the indicated injection shapes. As one would suspect this also plays into the weighting of particles in the multipactor simulation.
- **inject_interval** - This is the time in terms of **dt** between ejections from each cell. An important feature to note is if there are less particles than cells

Table 4. Comparison of weighting in terms as outputted by the ‘ice.stat’ file, the PART dump file and the theoretical output of equation 84 for the two dimensional NSC case of simulations, where the baseline value of the the cases has a current of 1, a Nx of 3, an inject of 1, an inject.interval of 1 and a resolution of 12000.

Property Changed	New Value	Particle Dump (C)	‘ice.stat’ (C)	Theoretical (C)
Baseline		7.94e-15	7.94e-17	7.94e-15
current	100	7.94e-13	7.94e-15	7.94e-13
Nx	50	4.76e-16	4.76e-18	4.76e-16
inject	7	1.13e-15	1.13e-17	1.13e-15
inject_interval	5	3.97e-14	3.97e-16	3.97e-14
Resolution	3000	3.17e-14	3.17e-16	3.17e-14

being injected at a time interval, the cell faces will randomly eject particles.

- dt - The timestep of the simulation defined by Equation 1 in Chapter I
- A_{Cell} - The area associated with a simulation unit grid (defined as dz^2).
- $A_{Emission}$ - The area of the emitting particle phase, defined as the dimension in the \hat{x} and \hat{y} directions.

Effective use of the Equations 83 and 84 enables efficient usage of computational resources within the simulation environment. However, care must be taken to balance the need for computational efficiency and the number of particles required to maintain statistical validity of the ICEPIC simulation .

When verifying Equations 83 and 84 a discrepancy was noticed in the values of the charge associated with the macroparticle in the ‘ice.stat’ file utilized for tracking particle count. By varying the parameters inside Equation 83 it was determined that the ‘ice.stat’ file always outputted macroparticle charges a factor of a hundred less than those predicted. These inconsistencies reported for the NSC case may be viewed in Table 4. Further, investigation confirmed that this inconsistency also occurs within the SC case. Both of these cases were ran for a two dimensional simulation. The PART dump files that describe particle data were also investigated for the particle charge

reported and as shown in Table 4, concurred with Equations 83 and 84. Rogers [19] previously reported a factor of a hundred reduction in present in the PART dump files for a previous version of ICEPIC. This previous discrepancy was associated with the two dimensional representation including a factor of 100 difference in scale size of the simulations. It has been hypothesized that the current version of ICEPIC has had this issue corrected, but a relic in the old version of the code leads to the default ‘ice.stat’ file still containing the factor of a hundred difference. This is supported in that the factor has does not seem to have an effect on the modeling process. Further confirmation of this explanation for the discrepancy comes from the fact that when three dimensions are simulated the ‘ice.stat’ particle charge reported is the same value predicted by Equations 83 and 84.

3.3 Results and Analysis

One of the main worries with window failure in HPM systems come from the power deposited on the the dielectric window. However, previous work by Lau indicates the electrons are not the primary cause of window failure, but trigger outgassing of impurities contained in the dielectric window [13]. Ions would then also become a constituent of the multipactor plasma delivering large amounts of power to the dielectric window. Neuber and Edminston have published results consistent with this theory in their attempts to mitigate dielectric window breakdown by preconditioning the dielectric material used in the window prior to experimentation [17].

Reflection by the multipactor electrons presents another problem. Even though this was briefly studied in Rogers work[19], reflected powers were taken over a much larger range of frequencies, in this research, giving a much more complete parameter space for assessing the reflection associated with multipactor. The results are indicated in Table 5.

Table 5. The maximum value of reflected power values measured by the “probe line” associated with E_{Ref} . The simulation results are compared to predicted values for reflection calculated from equations 73 and 75.

Frequency 1GHz		
$E(MV/m)$	Observed Power Reflection %	Theoretical Power Reflection %
1	0.04%	2.04 %
2	1.09%	2.56 %
3	4.00%	2.96 %
Frequency 2.45GHz		
$E(MV/m)$	Observed Power Reflection %	Theoretical Power Reflection %
1	0 %	1.11 %
2	0.02 %	1.81 %
3	0.08 %	2.25 %
Frequency 10GHz		
$E(MV/m)$	Observed Power Reflection %	Theoretical Power Reflection %
1	0 %	0.03 %
2	0 %	0.51 %
3	0 %	0.83 %

As indicated by the theory in Section 3.1, the reflection of power from the multipactor is a function of particle density, particle charge, the frequency of the propagating EM wave, and the particle emission velocity. As one can see the theoretical power reflected differs from the reported reflected power for a few of the simulations. The cause of these differences may be attributed to the particle distribution present within the simulation being different from the particle distribution associated with previous distributions reported by Valfells [22]. The theoretical values are based on the total count of particles present within the simulation, which may differ between the two dimensional and three dimensional simulation spaces.

IV. Conclusions and Future Work

4.1 Conclusions

The research conducted focused on mitigating the multipactor phenomenon and quantifying the effects associated with the reflection caused by the plasma. In order to mitigate the multipactor, susceptibility diagrams characterizing multipactor were reproduced within ICEPIC. During this process an important discrepancy was observed for the boundary curves. The origin of the discrepancy was traced to the original method of simulation not taking into account the magnetic field component of electromagnetic radiation propagating through the waveguide dielectric. For the high energy particles, the magnetic field imparts sufficient momentum to return particles to the dielectric surface even in the total absence of a bias electric field.

The remapping of the susceptibility curves taking into account the magnetic field indicates an opportunity to mitigate the initiation of multipactor with the application of a negative bias electric field. The magnitude of negative bias applied to the system would be much less than the corresponding positive bias based upon the lower boundary curve.

In quantifying the reflection associated with multipactor, a new analytic treatment was developed to determine the reflection coefficient from the particle density within the multipactor plasma. This analytic theory indicates that the reflection associated with multipactor would be negligible in agreement with previous results obtained by Fichtl and Rogers [8] [19]. The simulation in ICEPIC agreed for lower electric field amplitudes associated with the plane wave normal to the dielectric. However, the analytic and simulated results differed warranting further investigation.

4.2 Future Work

The research warrants further investigation in using a negative bias as a means of multipactor mitigation. Further simulations need to be conducted characterizing the new susceptibility diagrams for various materials, taking into account secondary emission properties associated with different materials. These new susceptibility diagrams need to include boundary curves associated with the lower and upper crossover energies present in the secondary electron emission curve. New research needs to also investigate methods of implementing a negative bias field into a real world applications. The implementation needs to provide a bias at a level that will prevent multipactor initiation while also not interfering with the propagation of electromagnetic radiation through the microwave dielectric. Spaulding is currently pursuing this study [21].

In order to better characterize reflection in actual microwave systems, simulations also need to be run for time periods consistent with those present in an actual HPM system. Modeling done was usually performed over 10 *ns* whereas in an actual system microwave pulses last in the 100–300 *ns* scale. Within the simulations that considered space charge, the total particle count of the simulation was observed to grow throughout the entirety of the simulation, indicating that power deposited on the window and reflected power would be greater than values at earlier times. Characterization of the overall particle growth as a function of the amplitude and frequency of propagating microwave radiation would allow for the forecasting of these values while avoiding the computational requirements in simulating such large time scales.

Other mitigation attempts should also be explored, such as attempts at modifying the geometry of the waveguide dielectric. Previous work accomplished by Rogers [19] in creating susceptibility curves in MATLAB[®] and Spaulding [21] have indicated that such attempts would prove fruitful in preventing the initiation of multipactor. In

particular creating simulations within ICEPIC characterizing the growth and decay of multipactor when the incident plane wave is off normal to the dielectric for the space charge case would be very effective in showing the benefits of such a mitigation method.

Within the research the “bowtie” curves have proven to be an effective means at understanding the time evolution of multipactor along the waveguide dielectric. Looking at the variation in the “bowtie” curve for higher microwave field amplitudes to analyze the coupling effect with space charge and reflection would also prove useful in understanding the dynamic evolution of multipactor in the system. By observing the electric field perpendicular and parallel within various areas of the electron cloud, the spatial distribution of the reflection into the multipactor could also be better quantified.

Bibliography

1. New world vistas, air and space power for the 21st century. Directed Energy Volume, Science Advisory Board Study, December 1995.
2. Defense technology area plan. Director, Defense Research and Engineering, January 1997.
3. L. Ang, Y. Lau, R. Kishek, and R. Gilgenbach. Power deposited on a dielectric by multipactor. *IEEE Transactions on Plasma Science*, 26(3):290–295, June 1998.
4. Robert J Barker and Edl Schamiloglu, editors. *High Power Microwave Sources and Technologies*. Institute of Electrical and Electronics Engineers Inc, Piscataway, New Jersey, 2001.
5. M. T. Bettencourt, J. D. Blahovec, and L. Bowers. *ICEPIC v. Feb11b User's Manual*. Directed Energy Directorate, High-Powered Microwave Division, Center for Plasma Theory and Computation, February 2011.
6. C.K. Birdsall and A.B. Langdon. *Plasma Physics Via Computer Simulation*. Adam Hilger, Philadelphia, Pennsylvania, 1991.
7. W.C. Brown. The history of power transmission by radio waves. *IEEE Transactions on Microwave Theory and Techniques*, 32(9):1230–1242, September 1984.
8. Christopher Fichtl. Self-consistent simulation of multipactor discharges at hpm dielectric windows. Technical report, Air Force Research Lab, February 2007.
9. M. Fox. *Optical Properties of Solids*. Oxford University Press, Great Clarendon Street, Oxford, 2 edition, 2011.
10. J. Franklin. *Classical Electromagnetism*. Pearson Education, 1301 Sansome St. San Francisco, CA 94111, 1 edition, 2005.
11. D. Hemmert, A. Neuber, J. Dickens, H. Krompholz, L.L. Hatfield, and M Kristiansen. Microwave magnetic field effects on high-power microwave window breakdown. *IEEE Transactions on Plasma Science*, 28(3):472–477, June 2000.
12. H. Kim and J. Verboncoeur. Time-dependent physics of a single-surface multipactor discharge. *Physics of Plasmas*, 12(123504):1–7, September 2005.
13. H.C. Kim, J.P. Verboncoeur, and Y.Y. Lau. Modeling rf window breakdown: from vacuum multipactor to rf plasma. *Institute of Electrical and Electronics Engineers, Inc.*, 14(4):766–773, 2007.
14. R. A. Kishek, Y. Y. Lau, L. K. Ang, A. Valfells, and R. M. Gilgenbach. Multipactor discharge on a dielectric. *Phys. Rev. Letter*, 80(1):193–196, 1998.

15. R. A. Kishek, Y. Y. Lau, L. K. Ang, A. Valfells, and R. M. Gilgenbach. Multipactor discharge on metals and dielectrics: Historical review and recent theories. *Phys. Plasmas*, 5:2120–2126, 1998.
16. A. Neuber, J. Dickens, D. Hemmert, H. Krompholz, L.L. Hatfield, and M. Kristiansen. Window breakdown caused by high-power microwaves. *IEEE Transactions on Plasma Science*, 26(3):296–301, June 1998.
17. A.A. Neuber, G.F. Edminston, J.T.Krile, H. Krompholz, J.C. Dickens, and M. Kristiansen. Interface breakdown during high-power microwave transmission. *IEEE Transactions on Magnetism*, 43(1):496–500, January 2007.
18. J. M. Osepchuk. A history of microwave heating applications. *IEEE Transactions on Microwave Theory and Techniques*, 32(9):1201–1224, September 1984.
19. Neil Rogers. Electron multipactor theory review, comparison and modeling of mitigation techniques in icepic. Master’s thesis, Air Force Institute of Technology, Wright Patterson Air Force Base, Ohio, 2009.
20. Vladimir Semenov, Elena Rakova, Nina Zharova, Dan Andeson, Mietek Lisak, and Jerome Puech. Simulations of the multipactor effect in hollow waveguides with wedge-shaped cross section. *Physical Review Special Topics*, 13(10):0222004–1–0222004–6, 2010.
21. J. C. Spaulding. Prevention of electron multipactor in high power microwave weapons, 2012. Private Communication.
22. A. Valfells, H.P. Verboncoeur, and Y.Y. Lau. Space-charge effects on multipactor dielectric. *Plasma Science, IEEE Transactions on*, 28(3):529–536, 2000.
23. J.R.M. Vaughan. Multipactor. *Electron Devices, IEEE Transactions on*, 35(7):1172–1180, 1988.
24. J.R.M. Vaughan. A new formula for secondary emission yield. *Electron Devices, IEEE Transactions on*, 36(9):1963–1967, 1989.

Vita

Lt Robert Lloyd was born in Lubbock, TX. After graduating from North Platte High School in 2007, he then attended the Air Force Academy, graduating in 2011. He then entered graduate school at the Air Force Institute of Technology (AFIT) where he is currently completing his Master's Degree. His next assignment will be for AFRL at Kirtland AFB, New Mexico.

REPORT DOCUMENTATION PAGE			<i>Form Approved</i> OMB No. 0704-0188		
The public reporting burden for this collection of information is estimated to average 1 hour per response, including the time for reviewing instructions, searching existing data sources, gathering and maintaining the data needed, and completing and reviewing the collection of information. Send comments regarding this burden estimate or any other aspect of this collection of information, including suggestions for reducing this burden to Department of Defense, Washington Headquarters Services, Directorate for Information Operations and Reports (0704-0188), 1215 Jefferson Davis Highway, Suite 1204, Arlington, VA 22202-4302. Respondents should be aware that notwithstanding any other provision of law, no person shall be subject to any penalty for failing to comply with a collection of information if it does not display a currently valid OMB control number. PLEASE DO NOT RETURN YOUR FORM TO THE ABOVE ADDRESS.					
1. REPORT DATE (DD-MM-YYYY) 21-03-2013		2. REPORT TYPE Master's Thesis		3. DATES COVERED (From — To) Aug 2011-Mar 2013	
4. TITLE AND SUBTITLE Multipactor Discharge in High Power Microwave Systems: Analyzing Effects and Mitigation through Simulation in ICEPIC				5a. CONTRACT NUMBER	
				5b. GRANT NUMBER	
				5c. PROGRAM ELEMENT NUMBER	
6. AUTHOR(S) Lloyd, Robert, L, 2d Lt, USAF				5d. PROJECT NUMBER	
				5e. TASK NUMBER	
				5f. WORK UNIT NUMBER	
7. PERFORMING ORGANIZATION NAME(S) AND ADDRESS(ES) Air Force Institute of Technology Graduate School of Engineering and Management (AFIT/ENY) 2950 Hobson Way WPAFB OH 45433-7765				8. PERFORMING ORGANIZATION REPORT NUMBER AFIT-ENP-13-M-22	
9. SPONSORING / MONITORING AGENCY NAME(S) AND ADDRESS(ES) AFRL/RDHE (Dr. Nathaniel Lockwood) 3550 Aberdeen Ave SE Kirtland AFB, NM 87117-5776 246-1888, Nathaniel.Lockwood@kirtland.af.mil				10. SPONSOR/MONITOR'S ACRONYM(S) AFRL/RDHE	
				11. SPONSOR/MONITOR'S REPORT NUMBER(S)	
12. DISTRIBUTION / AVAILABILITY STATEMENT APPROVED FOR PUBLIC RELEASE; DISTRIBUTION UNLIMITED					
13. SUPPLEMENTARY NOTES This material is declared a work of the U.S. Government and is not subject to copyright protection in the United States.					
14. ABSTRACT Single surface multipactor in high power microwave systems was investigated computationally and analytically. The research focused upon understanding the cause and parametric dependence of the multipactor process leading to suggested methods of mitigation. System damage due to reaction was also assessed. All simulations were performed using the PIC code developed by AFRL, known as ICEPIC. In recreating the susceptibility curves that define regions of multipactor growth and decay, a discrepancy was found between previous published results and those observed in the current simulation. This was attributed to previous simulations not accounting for the magnetic component in the electromagnetic radiation incident on the dielectric window. By surveying different static magnetic and electric fields both parallel and perpendicular to the dielectric, revised susceptibility curves were determined. An analytic method confirmed the origin of the discrepancy. The reflection of the waveguided radiation by the multipactor electrons degrades the output and may damage the microwave source. A theory for the reflection resulting from multipactor was derived to aide in quantifying reflection. A plane wave was used to model incoming microwave radiation and the amplitude of the electric field in reflected and transmitted waves was measured for various frequencies of the incident plane wave.					
15. SUBJECT TERMS Multipactor, HPM, Microwave, Reflection, Susceptibility Diagram					
16. SECURITY CLASSIFICATION OF:			17. LIMITATION OF ABSTRACT UU	18. NUMBER OF PAGES 67	19a. NAME OF RESPONSIBLE PERSON Dr. William F. Bailey ENP
a. REPORT U	b. ABSTRACT U	c. THIS PAGE U			19b. TELEPHONE NUMBER (Include Area Code) (937) 255-3636, x4501; william.bailey@afit.edu